

AN EQUATION OF STATE FOR LOW-MASS STARS AND GIANT PLANETS

D. SAUMON,^{1,2} G. CHABRIER,³ AND H. M. VAN HORN⁴*Received 1994 October 27; accepted 1995 February 2*

ABSTRACT

We present new equations of state (EOS) for hydrogen and helium, intended for applications to low-mass stars ($M < 1 M_{\odot}$), brown dwarfs, and giant planets. They cover the range $2.10 < \log T(\text{K}) < 7.06$ and $4 < \log P(\text{dyn cm}^{-2}) < 19$ and include new physical treatments of partial dissociation and ionization caused by both pressure and temperature effects. The hydrogen EOS is based on a careful study of nonideal interactions. In the case of helium, the principal features of the EOS physics are retained in a simplified model. The calculation is based on the free energy minimization method, and a detailed account of the physical model has been published elsewhere. Mixtures of hydrogen and helium are obtained with the additive volume rule and an additional ideal entropy-of-mixing term. In this paper, we present extensive tabular results for both the H and He EOS, together with a critical analysis. Part of this analysis is based on a comparison with other EOS commonly used in astrophysics. Both EOS everywhere satisfy the requirements of thermal and mechanical stability and are thermodynamically consistent over most of the phase diagram. A complete set of the tables is available in the AAS CD-ROM Series, Vol. 5, and by anonymous FTP.

Subject headings: equation of state — planetary systems — stars: interiors — stars: low-mass, brown dwarfs

1. A BRIEF HISTORY OF EQUATIONS OF STATE

The richness of stellar phenomena exposed by modern observational techniques calls for a quantitative understanding of more subtle, “second-order” effects in stellar structure and evolution. Examples of phenomena requiring accurate modeling of the underlying physics include the solar oscillation spectrum, the solar neutrino problem, stellar pulsations, and the abundances of elements in the photospheres of white dwarfs. Recent progress in infrared technology, together with the advent of new space observatories and of large ground-based telescopes, is fostering a substantially increased interest in theoretical studies of very low mass stars and of substellar brown dwarfs. Modeling these objects demands an understanding of the properties of matter under more extreme conditions than found in normal stars.

Many astrophysical problems require knowledge of the properties of matter at or near thermodynamic equilibrium. The thermodynamic properties of a fluid are characterized by the equation of state (EOS), which uniquely determines the pressure and all other thermodynamic quantities as functions of density and temperature, and which directly enters the equations of stellar evolution. The pressure $P(\rho, T)$ and the entropy $S(\rho, T)$ appear explicitly in these equations and dictate the mechanical and thermal equilibria of the star, respectively. Beyond the fact that an equation of state is necessary

to compute a stellar model, the quantitative understanding of “subtle” stellar phenomena depends, sometimes sensitively, on the assumed EOS (cf. Däppen 1994).

The complexity of an EOS calculation increases considerably when nonideal effects are compounded with the chemical reactions associated with partial dissociation and ionization equilibria. In fact, such calculations can only be performed numerically, and the results are usually presented in tabular form. Historically, the Lawrence Livermore National Laboratory and the Los Alamos National Laboratory have invested considerable effort in the development of tabular equations of state which are frequently used in astrophysical applications. Most of these EOS are based on the free-energy minimization technique (discussed in § 2.2) which was pioneered by Harris (1959) and by Harris, Trulio, & Roberts (1960). The method was significantly expanded to include a more sophisticated treatment of nonideal effects in H by Graboske, Harwood, & Rogers (1969) and by Fontaine, Graboske, & Van Horn (1977; hereafter, FGVH) who also studied He and C. In a similar vein, Magni & Mazzitelli (1979) generated a model for the EOS of mixtures of H and He. In an independent effort, with an altogether different set of approximations, Kerley (1972) developed a deuterium EOS from which an approximate H EOS can be obtained by density scaling. Numerical simulations of dense plasmas began in earnest in the early 1970s and have progressed ever since. Lamb (1974) and Lamb & Van Horn (1975) developed a model for the dense, fully ionized, strongly coupled Coulomb fluid and solid found in the cores of white dwarfs. The deep interiors of giant planets consist of metallized H and He and the interesting and complex thermodynamics of this binary Coulomb fluid were studied by Stevenson (1975), by Stevenson & Salpeter (1977), and in a series of paper by Hubbard & DeWitt (1985 and references therein). Marley & Hubbard (1988) integrated this effort with the recent experimental work on dense molecular hydrogen to generate

¹ Hubble Postdoctoral Fellow.

² Department of Planetary Sciences, University of Arizona, Tucson, AZ 85721 (dsaumon@lpl.arizona.edu).

³ Groupe d’Astrophysique (CNRS), Ecole Normale Supérieure, 46 Allée d’Italie, 68364 Lyon Cedex 07, France (chabrier@physique.ens-lyon.fr).

⁴ Department of Physics and Astronomy, University of Rochester, Rochester, NY 14627; currently on leave in the Division of Astronomical Sciences, National Science Foundation, 4201 Wilson Boulevard, Arlington, VA 22230 (hvanhorn@nsf.gov).

an EOS applicable to both the molecular envelope and the metallic interior of Jovian planets. In another series of papers, Rogers developed an EOS for stellar envelopes using the so-called activity expansion. This work is part of an effort dedicated to improving stellar opacities and to providing a consistent calculation of opacities and EOS (see Rogers 1994 and references therein). The most recent development in astrophysical EOS is the work of Mihalas, Hummer, & Däppen (Hummer & Mihalas 1988; Mihalas, Däppen, & Hummer 1988; Däppen et al. 1988) which returns to the free-energy-minimization technique, but with a much-improved treatment of the bound states of atoms and molecules interacting with their neighbors.

The past decade has seen tremendous progress in our understanding of dense matter physics, on both the experimental and theoretical fronts. Recent experiments on hydrogen and deuterium have led to the determination of the H_2 - H_2 potential down to separations of $\approx 1.5 \text{ \AA}$ (Ross, Ree, & Young 1983; Duffy et al. 1994). Equations of state for dense plasmas are now becoming well understood, thanks in part to progress in computer technology, which has permitted simulations of ever-increasing complexity. Several theoretical schemes have been proposed to derive accurate equations of state for fully ionized hydrogen (Ichimaru, Iyetomi, & Tanaka 1987; Chabrier 1990; Stolzman & Blocker 1994), partially ionized hydrogen (Perrot, Furutani, & Dharma-wardana 1990; Tanaka, Yan, & Ichimaru 1990; Chihara 1991a,b; Farouki & Hamaguchi 1994; Perrot & Dharma-wardana 1994), and for helium (Perrot et al. 1990). These theories, however, are valid only for fully or strongly ionized plasmas and break down for plasmas in which a significant number of electrons occupy bound states. These studies have demonstrated the great utility of different approximations for the computation of plasma properties. In particular, when a sample of any substance is sufficiently compressed, atoms (or molecules) are so closely packed that the exclusion principle promotes bound electrons into conducting states (for hydrogen, this occurs near 1 g cm^{-3}). This “pressure ionization” represents a thorny problem in the calculation of an equation of state, which is often avoided by simply interpolating between atomic and fully ionized limits. However, recent advances in statistical physics offer the opportunity for significant improvements in our understanding of this poorly understood phenomenon, and one of the goals of the present work is to incorporate this effect in a self-consistent treatment of the EOS.

It was first suggested independently by Wigner & Huntington (1935) and by Landau & Zeldovitch (1943) that pressure ionization may occur discontinuously through a first-order phase transition. Their qualitative argument was based on the drastically different natures of the interaction potentials in metals (weakly repulsive electron-screened Coulomb potentials) and in insulators (strongly repulsive hard-sphere potentials). The calculation becomes a challenge, requiring the incorporation of quantum mechanics for the electrons, an adequate treatment of the bound states of the atomic and molecular species in the dense fluid, and a careful treatment of the interactions among the species. The theoretical tools required to tackle this problem were largely developed by Ebeling and collaborators (Kraeft et al. 1986), and the first quantitative attempt to demonstrate the possibility of the aforementioned

phase transition in hydrogen, the so-called “plasma phase transition” (PPT), was derived by Ebeling & Richert (1985). Although their work was based on a very approximate treatment of the interactions, it motivated further detailed calculations, and in particular the work by Saumon & Chabrier (1991, 1992, hereafter SC1 and SC2, respectively) who derived a complete phase diagram for fluid hydrogen at high density.

In this paper, we present new EOS tables for pure H and pure He in which the nonideal effects are carefully included. In particular, pressure ionization of hydrogen has been explicitly treated. The EOS tables cover a pressure and temperature range appropriate for low-mass stars ($M < 1 M_\odot$), brown dwarfs, and giant planets. The EOS of H and He are discussed separately in §§ 3 and 4, respectively. The generation of the large EOS tables is described in detail in § 5. The thermodynamics of H/He mixtures can be obtained from compositional interpolation between the pure cases using the method described in § 6. Representative thermodynamic surfaces are presented and discussed in § 7, and § 8 addresses the constraint of thermodynamic consistency. Section 9 is devoted to an inter-comparison of several H EOS, a useful way of establishing their relative merits and flaws.

2. GENERAL CONSIDERATIONS

2.1. *Chemical and Physical “Pictures”*

Equation-of-state models can be divided into two broad categories (see Hummer & Mihalas 1988 for a detailed discussion). In the *physical picture*, only “fundamental” particles are considered (electrons and nuclei), which interact through Coulomb potentials. In principle, one would like to solve the Schrödinger equation for such a system using a quantum-statistical many-body theory, obtaining a spectrum of bound electronic states, forming “atoms” and “molecules” with density-dependent eigenvalues, together with free electronic states. This approach effectively solves the quantum problem simultaneously with statistical mechanics. It is appealing since it corresponds to our intuitive conception of the behavior of matter and is formally exact. It has been applied to partially ionized plasmas in the regime of weak ion-ion Coulomb coupling (Rogers 1981, 1984; see also Alastuey 1994 and Alastuey, Cornu, & Perez 1994). However, although the physical picture probably offers the most rigorous treatment, the calculation of an EOS using this approach is a formidably complex problem. It has not been applied to the relatively low temperatures and high densities relevant to the phenomenon of pressure ionization because the physical theories are based on an expansion which cannot converge in this regime.

On the other hand, the *chemical picture* assumes that bound configurations, such as atoms and molecules, retain a definite identity and interact through pair potentials. This amounts to solving the quantum problem first (with a heuristic approach) and then applying statistical mechanics to populate available states. This approximation has a serious drawback. At densities corresponding to pressure ionization, the electrons in bound configurations become delocalized, pair potentials become meaningless and consequently, bound species lose their identity. Nevertheless, the chemical picture emerges as a useful alternative in view of the practical limitations of the physical picture.

2.2. Free-Energy Minimization Technique

Our EOS models for H and He are within the framework of the chemical picture and based on the *free-energy minimization* (FMIN) technique which is well described by Graboske et al. (1969), FGVH, and Hummer & Mihalas (1988). The approach is particularly simple: Given a mathematical model for the Helmholtz free energy $F(V, T, \{N_i\})$ of the system as a function of the total volume V , temperature T , and particle numbers N_i for each species i , the chemical equilibrium of the mixture is obtained by minimizing F at fixed V and T , subject to the stoichiometric constraints imposed by the chemical reactions taking place in the system. This fixes the set $\{N_i\}$, and the pressure P and entropy S can then be calculated by differentiation of the free energy with respect to V and T , respectively, at fixed $\{N_i\}$. Exact expressions for these so-called first derivatives of the free energy are formally given by (Reichl 1980, p. 37):

$$P = - \left. \frac{\partial F}{\partial V} \right|_{T, \{N_i\}}, \quad S = - \left. \frac{\partial F}{\partial T} \right|_{V, \{N_i\}} \quad (1)$$

The specific heats, compressibility, thermal expansion coefficients, adiabatic gradients, etc., are obtained by further differentiating P and S with respect to V and T and constitute the second derivatives of the free energy. Note that in this case, the $\{N_i\}$ are not kept constant during the differentiation but allowed to vary with V and T according to the FMIN solution for the chemical equilibrium. Unfortunately, differentiation amplifies the features and defects in F , and since the second derivatives are usually obtained numerically, they are prone to numerical noise.

The FMIN method becomes truly useful when the grand partition function \mathcal{Z} of the system is written as the product of kinetic, internal, and configurational contributions:

$$\mathcal{Z} = \mathcal{Z}_{\text{kin}} \mathcal{Z}_{\text{int}} \mathcal{Z}_{\text{conf}} . \quad (2)$$

A physical discussion of the four approximations leading to this factorizability is given in FGVH. In practice, small deviations from exact factorizability are usually accommodated by corrections based on expansions in terms of a small parameter. However, when the particles of the system interact strongly, the spectrum of bound states is affected and \mathcal{Z}_{int} and $\mathcal{Z}_{\text{conf}}$ can no longer be factorized. Similarly, the bound state configuration determines the interaction potentials and modifies $\mathcal{Z}_{\text{conf}}$. In the FMIN procedure, the total partition function is nevertheless assumed to be factorizable, with some modification employed for the spectrum of bound states entering the internal partition function \mathcal{Z}_{int} based on the interaction potentials. Many different treatments of this problem have been used, some very crude and with little statistical mechanical consistency, some quite sophisticated. There is no formally exact treatment, however, and this is the source of many disagreements between EOS computed with this method.

Despite this shortcoming, the FMIN technique has several powerful advantages. In principle, it ensures thermodynamic consistency of the resulting equation of state. All the physics and approximations appear at the outset in the free energy model and are therefore quite visible. No additional approxi-

mations are required. Contrary to expansion techniques, contributions with strongly nonlinear dependences on density or temperature can be included with no additional effort. Under the assumption of factorizability, the free energy model becomes a sum of terms, each involving a different physical contribution. This is extremely convenient, as each term becomes a subroutine in the EOS code. Terms can be added, removed, and modified with ease. Hummer & Mihalas (1988) point out that this method will work for *any* free energy model. However, because the validity of the resulting EOS is hard to establish, unless it violates fundamental constraints or known limits, great care must be taken in constructing the free-energy model to ensure statistical mechanical consistency.

2.3. Constraints on Equations of State

The EOS is subject to the fundamental thermodynamic constraints of mechanical and thermal stability,

$$\left. \frac{\partial P}{\partial V} \right|_{T, \{N_i\}} < 0, \quad \left. \frac{\partial S}{\partial T} \right|_{V, \{N_i\}} > 0, \quad (3)$$

respectively, and of thermodynamic consistency, e.g.,

$$\left. \frac{\partial P}{\partial T} \right|_{V, \{N_i\}} = \left. \frac{\partial S}{\partial V} \right|_{T, \{N_i\}} . \quad (4)$$

In equations (3) and (4), the $\{N_i\}$ need not be held constant during differentiation provided that they have the values imposed by the condition of chemical equilibrium. This last constraint reflects the fact that $P(V, T)$ and $S(V, T)$ are derived from the same thermodynamic potential F ; similar relations hold among the mixed derivatives of other thermodynamic potentials. Violations of these constraints point to potential problems or flaws in the EOS, but an EOS which satisfies them is not necessarily accurate. In particular, the FMIN method *guarantees* thermodynamic consistency for *any* free-energy function $F(V, T, \{N_i\})$.

Although great progress is currently being made in laboratory measurements, most astrophysically interesting regimes are still weakly constrained by experimental data. While any theoretical EOS should be required to reproduce the appropriate experimental results, it remains true that the validity of an EOS can only be established in an indirect fashion. It should, of course, reproduce known asymptotic limits. Computer simulations also provide useful but limited tests for theoretical equations of state. Finally, equations of state can be compared with each other in the light of the physics included in the underlying models. This helps to establish the relative merits of the EOS and of the approaches used, as well as to map our progress toward a realistic description of the behavior of matter under extreme conditions.

3. EQUATION OF STATE FOR HYDROGEN

3.1. Hydrogen Phase Diagram

The simplified phase diagram for hydrogen shown in Figure 1 helps to make a few basic points. In the low-density, low-temperature region, hydrogen is essentially neutral and forms

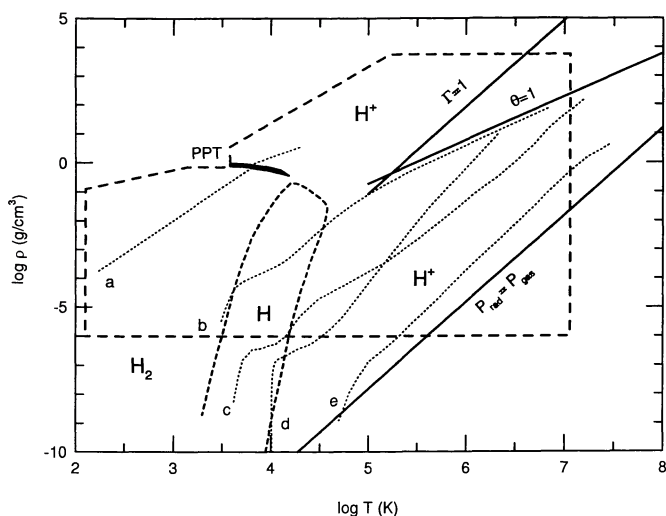


FIG. 1.—Phase diagram of hydrogen. The area delimited by the long-dashed line shows the coverage of the present EOS calculation for H.

atoms and molecules. Molecules dominate at low temperatures⁵ ($\log T \lesssim 3.5$), and they dissociate into atoms as the temperature is raised. At still higher temperatures, atoms ionize to form a low-density plasma of protons and electrons. The dashed curve delimiting these three regions indicates a degree of dissociation (or ionization) of 50%. At densities above $\log \rho \approx -2$, atoms and molecules interact strongly and form a nonideal fluid. In addition, the Saha equations for ionization and dissociation equilibria become completely inappropriate for $\log \rho > -1$, so that it is not possible to estimate the chemical equilibrium in this dense fluid with simple theories. At even higher densities, near $\log \rho = 0$ for hydrogen, the mean distance between H atoms becomes comparable to twice the value of the Bohr radius, and the electronic wave functions of neighboring atoms overlap. The electrons are forced into unbound states, and the fluid becomes a pressure-ionized plasma. Our calculation of pressure ionization (SC2) reveals that pressure-ionization of hydrogen may not be a gradual process at all temperatures but may occur discontinuously through a first-order phase transition, the so-called “plasma phase transition” (PPT). The metastable region of this transition is shown by the heavy curve labeled “PPT,” which ends at a critical temperature of $\log T_c = 4.185$.

Two important issues pertaining to the plasma are the degree of electron degeneracy and the strength of the Coulomb coupling between the charged particles. Above the solid line labeled $\theta = 1$, where $\theta \equiv k_B T / \epsilon_F$, the zero-temperature Fermi energy ϵ_F of the electrons is larger than $k_B T$, and they are therefore degenerate. Protons, on the other hand, remain classical over most of this diagram. Above the line $\Gamma = 1$, where $\Gamma \equiv e^2 / ak_B T$, nonideal Coulomb effects play an important role. In this regime, the electrostatic potential energy between two protons, e^2/a , where e is the proton charge and a is the mean interpar-

ticle distance, becomes larger than their kinetic energy, $k_B T$. A third plasma parameter, which is related to the electron density, is $r_s = a_e / a_0$, where a_e is the mean separation between electrons and a_0 is the Bohr radius. At intermediate temperatures ($\log T \approx 5$) and at densities $\log \rho \approx 0$, temperature- and pressure-ionization are of comparable importance. In this regime, thermal excitation of hydrogen atoms is significant, and they are immersed in a moderately coupled plasma ($\Gamma \approx 1$) in which the electrons are partially degenerate ($\theta \approx 1$). This regime is particularly difficult to treat, because the internal levels of the atoms are strongly perturbed by the surrounding plasma. For most elements, this is the regime, along with pressure ionization, in which equations of state are most unreliable.

Electrons remain nonrelativistic throughout this diagram. On the other hand, at low densities and high temperatures, the radiation pressure P_{rad} becomes larger than the gas pressure, P_{gas} . Finally, the upper left part of Figure 1 represents conditions which are not realized in astrophysical contexts, where hydrogen is a molecular solid or possibly forms a Coulomb lattice.

Interior models of various hydrogen-rich objects are shown by dotted curves in Figure 1. The gaseous envelope of Jupiter is shown by the curve labeled “a.” The envelope is dominated by molecular hydrogen, and it passes through the region of pressure ionization. If the PPT calculated by SC2 actually occurs in nature, it should be found in the envelope of Jupiter. Just below the PPT, the dense molecular fluid becomes strongly nonideal due to the strongly repulsive intermolecular forces.

Curves b, c, and e represent main-sequence stars with masses of 0.3, 1, and 15 M_\odot , respectively. The 15 M_\odot star has the simplest EOS physics. It is fully ionized throughout its interior, and the plasma is very weakly coupled ($\Gamma \ll 1$). Electron degeneracy is also weak ($\theta \gg 1$). The contribution of radiation pressure is significant, however, and the ratio $P_{\text{rad}}/P_{\text{gas}}$ is roughly constant throughout the interior. The solar model c is both cooler and denser. Accurate modeling requires attention to relatively weak nonideal effects ($\Gamma \approx 0.1$) and partial electron degeneracy near the center. Recombination of the plasma into H atoms affects the structure near the surface. Low-mass stars, such as the 0.3 M_\odot model shown, probe more complex areas of the phase diagram. Electrons are partially degenerate throughout most of the star, and the electrostatic interactions in the plasma become significant. This model crosses the difficult regime where both Γ and θ are of order unity. In the outer part of the model, protons and electrons recombine to form atoms in a nonideal regime, and finally molecules form at the very surface. Brown dwarfs generally occupy the region between curves a and b.

Curve d is a 12,500 K DA white dwarf envelope, stratified into hydrogen-rich and helium-rich layers, surrounding a carbon core (H, He, and C, respectively). Only the outermost layer, consisting of pure hydrogen, is shown here. In this layer, hydrogen forms a weakly coupled, nondegenerate plasma. Atomic hydrogen is found at the very surface of the star. The relatively low densities and high temperatures characteristic of this layer indicate that nonideal effects in the EOS are of moderate importance.

⁵ Throughout this work, $\log T$ is the logarithm of the temperature in K, and $\log \rho$ is the logarithm of the mass density in g cm^{-3} .

3.2. Free-Energy Model for Hydrogen

We have developed a *single, unified* Helmholtz free-energy model to describe the EOS of hydrogen throughout the region bounded by the long-dashed line shown in Figure 1. In some limiting regimes, this model reduces to simpler forms which are computationally more expedient. The model is fully described by Saumon (1990), SC1, SC2, and Chabrier (1990). In these papers, the resulting EOS is compared with static and dynamic compression experiments, and certain aspects of the model are compared with computer simulations. Both types of comparisons demonstrate the viability of our model in the regimes where it can be tested.⁶

A presentation of the model and a justification of its approximations would be too lengthy to be reproduced here. Instead, we provide here only a brief summary of the main features and refer the interested reader to the papers cited above for details.

1. We consider the following species: H_2 , H , H^+ , and e . Species such as H^- , H_2^+ , and H_3^+ have very low abundances and have a negligible effect on the EOS.
2. The model is based on the chemical picture, and we assume factorizability of the partition function; classical particles statistics for H_2 , H , and H^+ ; and Fermi-Dirac statistics for the electrons.
3. We account for weak diffraction effects in the interactions between heavy particles through the Wigner-Kirkwood \hbar^2 correction.

We treat interactions between neutral particles as follows:

1. The configuration free energy for neutral particles is evaluated in the framework of the WCA fluid perturbation theory (Weeks, Chandler, & Andersen 1971a,b), after suitable modification for application to a binary mixture at high densities and temperatures. We consider only pairwise interactions.
2. We use an experimentally determined H_2 - H_2 potential, and ab initio H - H_2 and H - H potentials.

Interactions between charged particles are treated in the following way:

1. At high densities, the fluid is represented by a plasma of protons immersed in a *polarizable* electron background. In the limit of weak electron-proton coupling ($\log \rho \gtrsim -0.5$), this plasma can be approximated as the superposition of (1) a fluid of electron-screened ions, interacting through a *screened* Coulomb potential that includes the ion-ion and the ion-electron interactions, and (2) a background of rigid, degenerate electrons (Ashcroft & Stroud 1978). At very high densities, the one-fluid model describing the electron-screened ionic fluid, known as the screened one-component plasma model (SOCP), reduces to the well-studied one-component plasma model (OCP), a mixture of point ions immersed in a *rigid* electron background.

⁶ In the final stage of preparation of this paper, we learned that Holmes, Ross, & Nellis (1995) have measured for the first time the temperature of shock compressed H_2 and D_2 . Their result seem to indicate that the degree of pressure dissociation of H_2 is higher than predicted by the model presented here. This was anticipated to a certain degree by SC1 and SC2. A study of the consequence of these very recent measurements on the EOS is in progress.

2. The polarizability of the electron fluid is described by a density- and temperature-dependent dielectric function that includes a local field correction to take into account correlation effects between electrons beyond the random phase approximation (Chabrier 1990).

3. The thermodynamics of the SOCP is obtained by solving an integral equation, the so-called hypernetted chain equation. It reproduces the results of Monte Carlo simulations to better than 1%. It also recovers the well-known limiting behaviors of the OCP (limit of no screening, $r_s = 0$), the hot Thomas-Fermi model ($r_s \ll 1$, $\theta \ll 1$), and the one-component Debye-Hückel limit ($\Gamma \ll 1$, $r_s = 0$).

4. The thermodynamics of the quantum electron fluid includes exchange and correlation terms *at finite temperature* (Ichimaru et al. 1987).

5. For $r_s > 10$ ($\log \rho < -2.6$), electrons and protons are both weakly coupled and behave as classical particles. The one-component, dielectric formulation of the SOCP does not apply here, and we use a two-component plasma (TCP) model in which protons and electrons interact through Coulomb potentials modified to account for quantum diffraction effects at very short range. The latter modification prevents the well-known collapse of a classical gas composed of particles of opposite charges. This model recovers the appropriate two-component Debye-Hückel limit ($\Gamma \ll 1$, $r_s \gg 1$).

6. Interactions between charged particles and neutral atoms and molecules are described by a polarization potential (Kraeft et al. 1986). This potential is attractive at long range, where a charged particle feels the dipole it induces in the neutral particle. At short range, however, the force becomes strongly repulsive, and we approximate this by a hard-sphere potential.

The internal partition function (IPF) of an isolated atom is well known to be divergent. For this reason, the sum over bound states must be cut off in some appropriate way. Physically, such a cut off is justified by the interactions with neighboring particles. The FMIN method is weakly constrained in this respect, and the differences among the approaches that have been employed are often the source of internal inconsistencies and of disagreements between different equations of state. Regions of partial ionization and dissociation (cf. Fig. 1) are particularly sensitive to this aspect of the free-energy model. We have adopted the following treatment for bound states:

1. The energies of bound levels (H , H_2) are taken to be those of the isolated atom or molecule, and the effect of interparticle interactions is described with an "occupation probability" formalism (SC1; described in detail in Hummer & Mihalas 1988). All known excited electronic states of the H_2 molecule are included, with their respective vibrational and rotational levels. The internal partition function \mathcal{Z}_{int} , becomes

$$\mathcal{Z}_{\text{int}} = \sum_{n=0}^{\infty} g_n \omega_n \exp(-\epsilon_n/k_B T), \quad (5)$$

where g_n is the multiplicity of level n with energy ϵ_n , and $0 \leq \omega_n \leq 1$ is the occupation probability of the level. This approach offers a good level of consistency between the interaction terms and their effect on the internal partition function.

2. Occupation probabilities are computed from the part of the configuration energy that corresponds to the equivalent volume occupied by the neutral particles. This “excluded volume” contribution is the lowest-order approximation to the total configuration free energy.

3. The volume occupied by neutral particles is expressed in terms of equivalent hard sphere diameters for H_2 and H. These are computed from the interaction potentials with a temperature- and density-dependent thermodynamic criterion.

3.2.1. Plasma Microfield

The free-energy model for hydrogen described above can be improved in several ways. We are currently considering a number of such improvements. The most important of these involves the effect of charged particles on the bound states of hydrogen atoms. Interactions with neighboring particles, charged and neutral, affect the number of bound states of atoms and molecules. A proper treatment of this effect is essential for an accurate description of partial dissociation and ionization, particularly at larger densities ($\log \rho \geq -3$).

In its current form, our free-energy model only accounts for the effect of neutral particles on excited bound states. In reality, neighboring charged particles also affect the bound states, both through inelastic collisions with bound electrons and also through the fluctuating micro-electric field induced by their thermal motion. This microfield acts as a time-dependent perturbation on the Coulomb potential of the nucleus and can induce Stark ionization of the upper levels of an atom. Collisions and microfield effects on hydrogenic atoms are discussed in great detail by Hummer & Mihalas (1988), who conclude that for $\log \rho \leq -1.5$, the microfield is the dominant mechanism. Being caused by random thermal motions, the fluctuating microfield is described by a statistical distribution (see also Perrot & Dharma-wardana 1994). Hummer & Mihalas have adopted the $\Gamma = 0$ Holtzmark distribution, where Γ is again the Coulomb-coupling parameter defined above. We have found that this distribution, which does not account for the correlations among charged particles at $\Gamma > 0$, has much too strong an effect on the internal partition function and leads to spurious results for $\Gamma \approx 1$. Generating microfield distributions for finite Γ is computationally involved, and a suitable, parameterized form was not available when this EOS was computed. As a consequence, we have ignored the effect of the microfield

altogether, preferring to delay its inclusion until an adequate distribution function becomes available. The net effect of this omission is that, as the gas becomes thermally ionized, the bound states of an H atom are less affected by the neighboring particles than is the case when the atom is surrounded by neutral particles. As temperature-ionization proceeds (e.g., by raising T), the internal partition function for H is thus slowly repopulated, a nonphysical behavior. This creates a “tail” of residual atoms at the few percent level in the partial ionization zone. We shall return to this point in § 9.

3.3. “Plasma Phase Transition” (PPT)

The realistic description of a dense plasma and of the H_2 -H mixture provided by our model allows us to focus on the problem of pressure-ionization from both the high-density and the low-density sides. We found that the model described above becomes thermodynamically unstable in the regime of pressure ionization and exhibits the features of a first-order phase transition. We have computed the coexistence curve for this transition using the phase equilibrium conditions (SC2). The characteristics of the resulting phase transition are given in Table 1, and the corresponding metastable region is indicated in Figure 1. This “plasma phase transition” (PPT) indicates that pressure ionization is a *discontinuous* process. As with all first-order phase transitions, all thermodynamic quantities are discontinuous across the coexistence curve except for T , P and the chemical potentials.

Since ionization is known to be continuous along a high-temperature isotherm and that our model predicts discontinuous pressure-ionization at low temperatures, there must exist a critical value of the temperature, T_c , above which there is no transition. We find this critical point at $\log T_c = 4.185$, $\log P_c = 11.788$, and $\log \rho_c = -0.456$.

This transition separates a mostly nonionized phase dominated by H_2 molecules (phase I) from a partially ionized phase dominated by fluid metallic hydrogen (phase II) which lies at higher density. The degree of ionization in each phase is given in Table 1, where α is the fraction of all hydrogen nuclei which are in the form of H^+ .

We emphasize that this result does not stem from any special assumptions about pressure ionization built into the free-energy model. It appears “naturally” from our best effort to describe the behavior of hydrogen throughout the phase diagram.

TABLE 1
COEXISTENCE CURVE FOR THE PLASMA PHASE TRANSITION

$\log T$ (K)	$\log P$ (dyn cm ⁻²)	$\log \rho^I$ (g cm ⁻³)	$\log \rho^{II}$ (g cm ⁻³)	α^I	α^{II}	ΔS^a (k_B per proton)
3.70	12.330	-0.125	-0.036	3.77×10^{-4}	0.194	0.615
3.78	12.290	-0.155	-0.056	5.50×10^{-4}	0.211	0.590
3.86	12.210	-0.194	-0.097	8.23×10^{-4}	0.214	0.544
3.94	12.143	-0.237	-0.131	1.39×10^{-3}	0.228	0.508
4.02	12.053	-0.292	-0.187	2.49×10^{-3}	0.232	0.464
4.10	11.952	-0.367	-0.260	5.58×10^{-3}	0.229	0.421
4.18	11.800	-0.456	-0.420	5.81×10^{-2}	0.133	0.142
4.185	11.788	-0.456	-0.456	7.52×10^{-2}	7.52×10^{-2}	0

^a The change in entropy across the PPT is $\Delta S = S^{II} - S^I$.

SC2 investigated a variety of modified free-energy models, all of which lead to the same qualitative result. The EOS also reproduces known limits which bracket the PPT. Further, the behavior of the EOS at pressures above and below the regime of pressure ionization, where the EOS is quite reliable, suggests that something peculiar happens in the intermediate regime (Fig. 2 of SC2). In our model, the PPT apparently occurs because the screened Coulomb potential is much less repulsive than the H_2 - H_2 potential. As the system is compressed at low T , it collapses to a state which occupies a smaller volume in phase space. Despite these plausibility arguments, however, we emphasize that there is as yet no direct experimental evidence supporting the existence of the PPT.

3.3.1. A Flaw in the EOS

Just above the PPT, Table 1 shows that ionization is not complete in phase II. The model predicts a gradual increase of α as the density is raised in phase II, so that complete ionization is finally reached by a *second* but smaller, discontinuous jump. This second discontinuity occurs at $\log \rho \approx 0.4 \rightarrow 0.5$, depending on the temperature. There are conceptual and physical reasons to reject this feature of the EOS, while still maintaining the physical plausibility of the PPT. The reason is that this second discontinuity can be directly traced to an ad hoc feature of the potential we have used to describe the interactions between neutral particles. The prediction of the PPT, however, does not hinge on this feature, as discussed by Saumon (1990) and by SC2. Because it has no physical basis, we have removed this second discontinuity in the EOS by interpolating each computed isotherm between $\log T = 3.54$ and 4.66 over this narrow density range, to bridge the gap between phase II and the fully ionized plasma. We have interpolated S independently from P . A somewhat peculiar and definitely unphysical behavior remains in the interpolated entropy, leading to an undesirable feature in $\partial S / \partial \rho|_T$ which could not be eliminated.

3.4. Interpolation

Despite the quest for the metallization of hydrogen in the laboratory (cf. Mao & Hemley 1992 and references therein) and the observation of exciting phenomena revealing a rich phase diagram for this simplest of all elements, the PPT remains hypothetical. For this reason, we have also generated EOS tables in which we have interpolated across the entire regime of pressure ionization to remove all of the discontinuities associated with the PPT. The resulting EOS represents our best estimate of the thermodynamics of hydrogen, if we assume that pressure ionization occurs continuously. This interpolated EOS also provides a useful reference for studying the effects of the PPT in various astrophysical situations.

Interpolation of EOS surfaces in a bounded (ρ, T) domain is constrained by a number of requirements. Clearly, all first and second derivatives of the free energy with respect to ρ and T must be smooth and continuous at the boundaries. In addition, the interpolated EOS must satisfy the constraints of mechanical and thermal stability, as well as thermodynamic consistency (eqs. [3]–[4] above). After extensive experimentation with a variety of interpolation schemes, we have found that in practice, these constraints cannot all be met unless the interpolated region is expanded well into regions where we be-

lieve that the EOS is very reliable. This may be a further indication that something unusual actually does happen in the regime of pressure ionization.

The final interpolation scheme we have adopted compromises thermodynamic consistency by putting the emphasis on the accuracy of the $P(\rho, T)$ and $S(\rho, T)$ surfaces. To that end, we have kept the size of the interpolation region to a minimum. We used cubic splines along individual isotherms to interpolate $\log(P/\rho^2)$ and $\log S$ independently across the pressure-ionization region. The entropy is a very well behaved quantity and is easily interpolated. The pressure, however, is a more rapidly varying quantity, and it was necessary to assist the interpolation “manually” in order to avoid unreasonable behavior of the spline interpolant in some regions. The density range of the interpolation, which is the same for P and S , was adjusted separately for each isotherm to preserve as much of the original EOS as possible while still obtaining a well-behaved interpolated surface. The resulting interpolated region covers roughly the range $3.54 \leq \log T \leq 4.74$ and $-0.5 \leq \log \rho \leq 0.5$. Because second derivatives of the free energy are obtained by differentiating these new surfaces, the EOS is not thermodynamically consistent in this region, as expected. This issue is discussed in depth in § 8.

Another useful quantity which we have tabulated is the internal energy, U . Instead of interpolating U independently from P and S , and thereby introducing additional inconsistencies into the EOS, we have used the relation

$$\left. \frac{\partial U}{\partial T} \right|_V = T \left. \frac{\partial S}{\partial T} \right|_V, \quad (6)$$

so that the U and S surfaces are constructed to be consistent with each other. We start by interpolating $\log U$ along the coldest interpolated isotherm ($\log T = 3.54$), and we then fill the interpolated region by integrating equation (6) with respect to T . Due to numerical inaccuracies, the resulting U surface is not as smooth as the S surface, with typical errors of $\lesssim 4\%$. While derivatives of S can be expressed in terms of derivatives of U , more accurate results are obtained by differentiating the $S(\rho, T)$ surface.

4. EQUATION OF STATE FOR HELIUM

4.1. Helium Phase Diagram

Figure 2 shows the phase diagram of helium, identifying the same physical regimes as in Figure 1. Regimes dominated by He, He^+ , and He^{2+} , respectively, are separated by dashed lines which indicate a degree of ionization of 50% for each ionization stage. These chemical equilibrium curves do not extend into the high-density region, as their counterparts do in Figure 1 for H, because we have not addressed the problem of pressure ionization of helium, as we discuss in the next section. However, pressure ionization of helium probably occurs at densities ~ 10 – 50 g cm^{-3} . The dotted line labeled “a” is an envelope model for a DB white dwarf (pure helium composition) with $T_{\text{eff}} = 15,000 \text{ K}$ and $\log g = 8$. Due to the low opacity of atomic helium, which dominates the photosphere in this model, the envelope has a much higher density than the similar DA model shown in Figure 1. Consequently, electron degeneracy and

The parameter α is the dimensionless chemical potential for the free electrons, $\alpha = \mu_e/k_B T$, defined by

$$I_{1/2}(\alpha) = \frac{2}{3}\theta^{-3/2}, \quad (12)$$

where θ is the degeneracy parameter defined in § 3.1.

2. The configuration free energy F_{conf} arising from He-He interactions is computed with the variational form of fluid perturbation theory, which has been very successful in describing atomic and molecular fluids near the triple point. (A different form of fluid perturbation theory, the so-called WCA expansion, was used for the H₂-H fluid configuration energy in § 3.2.) Such theories are based on the fact that atomic and molecular interaction potentials have weak, usually attractive, tails at long range (typically $1/r^6$) and strongly repulsive cores at short range. This allows the separation of the potential into a “reference” part (the strongly repulsive core) and a “perturbation” part (the weak long-range tail). An expansion of the free energy is performed around the contribution arising from the “reference” part, which is almost always approximated by the free energy of a hard-sphere fluid. An excellent review of fluid perturbation theories can be found in Barker & Henderson (1976), and a summary is given in Saumon (1990). Here we use a modified variational fluid theory developed by Ross (1979), in which the reference potential is taken to be proportional to $1/r^{12}$ instead of a pure hard-sphere potential. This choice gives a better account of the softness of the repulsive core (which is *not* infinitely repulsive) and leads to better agreement with experimental results at high densities. In this formulation, we have

$$F_{\text{conf}} = F_{\text{SS}}(\eta) + \frac{N_1^2}{V} \int_{\sigma}^{\infty} \phi(r) g_{\text{HS}}(r, \eta) d^3r, \quad (13)$$

where $F_{\text{SS}}(\eta)$ is the free energy of the soft-sphere reference system (Ross 1979):

$$F_{\text{SS}}(\eta) = N_1 k_B T \left[\frac{\eta(4-3\eta)}{(1-\eta)^2} - \left(\frac{\eta^4}{2} + \eta^2 + \frac{\eta}{2} \right) \right], \quad (14)$$

which is expressed in terms of the hard-sphere fluid parameter, the so-called “packing fraction:”

$$\eta = \frac{\pi}{6} \frac{N_1}{V} \sigma^3, \quad (15)$$

where σ is the diameter of the hard sphere.

The second term on the right-hand side of equation (13) is the first term of the perturbation expansion. The pairwise interaction potential between He atoms, $\phi(r)$, is determined experimentally by shock-tube experiments (Nellis et al. 1984), and $g_{\text{HS}}(r, \eta)$ is the pair distribution function of the hard-sphere fluid (Smith & Henderson 1970; Verlet & Weis 1972). It can be shown that this expansion provides an absolute upper bound to the exact F_{conf} . In the variational form of the fluid perturbation theory, the hard-sphere diameter σ is determined by minimizing eq. (13).

At low temperatures and high densities, the de Broglie wavelength λ_{th} of a He atom becomes comparable to the range r_0 of

the potential $\phi(r)$. In this regime, He atoms no longer interact as classical point particles. This violates a key assumption underlying the formulation described above. When λ_{th}/r_0 is not too large, the quantum effects are weak, and they can be included to leading order by adding to F_{conf} the first nonvanishing term of the Wigner-Kirkwood \hbar^2 expansion to (Landau & Lifshitz 1980, p. 98):

$$F_{qm} = \frac{\hbar^2 N_1^2}{24 m_{\text{He}} V k_B T} \int_0^{\infty} \nabla^2 \phi(r) g_{\text{HS}}(r, \eta) d^3r. \quad (16)$$

3. Interactions between the charged particles are described by a simple Debye-Hückel potential. In our present calculation, we ignore the fact that He⁺ is not a point particle. This is not a bad approximation at low densities, since the radius of the this ion is small ($\approx a_0/2$). For $\log \rho \lesssim 0$, the particles are far enough apart so that they feel the Coulomb part of the interaction with He⁺ but not the very short range effect of the bound electron. The free energy is thus approximated by

$$F_{\text{DH}} = - \frac{k_B T V}{12 \pi \lambda_{\text{DH}}^3}, \quad (17)$$

where

$$\lambda_{\text{DH}} = \left(\frac{4 \pi e^2}{V k_B T} \sum_j Z_j^2 N_j \theta_j \right)^{-1/2} \quad (18)$$

is the generalized Debye screening length for a multicomponent plasma (DeWitt 1961). The sum is over all species of charged particles with charge Z_j , including electrons, and θ_j is a correction for degeneracy. For all ions, $\theta_j = 1$ and for electrons,

$$\theta_e = \frac{1}{2} \frac{I_{-1/2}(\alpha)}{I_{1/2}(\alpha)}. \quad (19)$$

In the nondegenerate limit, $\theta_e = 1$.⁷

The Debye-Hückel model of screening provides the correct limit for $\Gamma \ll 1$, but it overestimates Coulomb effects when the coupling becomes significant $\Gamma \approx 1$.

4. The bound states of He and He⁺ are included in the simplest possible way by ignoring all excited states. This is a good approximation so long as $\log T \lesssim 4.2$ for He and $\log T \lesssim 4.5$ for He⁺. This approximation does affect the location and the detailed properties of the partial ionization zone, but not dramatically. We adopt the ground state of the He atom as the zero point of energy. The internal free energy is given by

$$F_{\text{int}} = -k_B T \sum_{i=1}^3 N_i \ln \mathcal{Z}_i, \quad (20)$$

where

$$\mathcal{Z}_i = \sum_n g_n e^{-\epsilon_n/k_B T} \quad (21)$$

⁷ The factor $\frac{1}{2}$ in eq. (19) is missing in FGVH.

is the internal partition function for species i . Given the simplifying assumptions discussed above, we have

$$F_{\text{int}} = -k_{\text{B}}TN_2 \ln 2 + N_2\chi_1 + N_3\chi_2, \quad (22)$$

where $\chi_1 = 24.587$ eV and $\chi_2 = 79.003$ eV are the first and second ionization potentials for He (Allen 1973, p. 37). Since we consider only the ground state of the two bound species, the occupation probability formalism is unnecessary here.

This free-energy model is admittedly simple, but it nevertheless provides an excellent description of the thermodynamics of He in a large part of the phase diagram covered by our calculation (Fig. 2). In particular, for $\log T \lesssim 4.2$, where helium is entirely atomic or very weakly ionized (at very low density), it is very reliable up to the high-density limit of the calculation ($\log \rho \lesssim 0$) for these temperatures. The He-He potential we have used is based on experimental data that probes the He EOS in the range $\log T \leq 4.3$ and $-0.5 \lesssim \log \rho \lesssim -0.15$. By construction, the EOS resulting from this free-energy model reproduces the experimental data very well. (Nellis et al. 1984). For $\log \rho \gtrsim 1$, the SOCP model for the fully ionized fluid is very reliable, as is the Debye-Hückel treatment in the region where $\Gamma \lesssim 0.1$ and He is fully ionized (lower right part of the calculation).

The largest uncertainties in this model are found, not surprisingly, in the regimes of temperature and pressure ionization, up to the region where both Γ and θ are of order unity. Future improvements could include (1) the excited states of He and He^+ , in the occupation probability formalism; (2) the plasma microfield; (3) interaction potentials involving He^+ ; (4) a two-component plasma (TCP) model for the low-density plasma; and (5) a careful study of pressure ionization. Work in this direction is under progress (Aparicio & Chabrier 1995).

4.3. Interpolation

Since the free energy model for He is inadequate to address the problem of pressure ionization, we interpolated to bridge the gap between the low- and high-density parts of the EOS, just as we have done for hydrogen (§ 3.4). In particular, we used cubic spline functions to interpolate P and S separately along isotherms, and we computed the internal energy U in the interpolation region by integrating equation (6). We adjusted the boundaries of this region to provide the smoothest possible interpolation, while keeping the density range as narrow as possible. The interpolation region ranges roughly from $\log \rho = -0.5$ to 1; the exact shape is discussed further in § 8.

5. CALCULATION OF THE EOS TABLES

Since our free-energy models are computationally expensive, especially for the case of hydrogen, it is not possible to use the EOS code “on line” in any practical application. The alternative is to generate a table of thermodynamic quantities for each element covering the density and temperature domain of interest and to rely on an accurate interpolation procedure in that table. In principle, high accuracy can be achieved by using a fine grid for the table. However, the computational effort increases with grid resolution, as does the amount of

memory occupied by the table in the application code. Our choices of boundaries and grid spacings, respectively, are

$$2.10 \leq \log T \leq 7.06, \quad -6.00 \leq \log \rho \leq 3.75, \quad (23)$$

$$\Delta \log T = 0.08, \quad \Delta \log \rho = 0.25. \quad (24)$$

The exact shapes of the areas in the $(\log T, \log \rho)$ plane covered by the calculations are indicated in Figures 1 and 2 for hydrogen and helium, respectively. We did not compute the EOS in the upper left corner of each phase diagram, because our models are inadequate to describe the atomic or molecular solids or the Coulomb lattice state found under these conditions. These phases are unlikely to be interesting from an astrophysical point of view. The boundaries of these regions were determined by studying the behavior of each EOS in the light of the limitations of the corresponding free-energy model and of fundamental constraints on the thermodynamics.

In regions where the EOS is a sensitive function of the density, in regimes where the code had difficulties in converging to chemical equilibrium, and also to “resolve” the PPT, we decreased $\Delta \log \rho$ to a minimum value of $\Delta \log \rho = 0.05$. After computation of the tables, we found that the adopted $\log T$ spacing was somewhat too coarse for a reliable interpolation in the partial temperature-ionization zones. Several additional isotherms were thus added in these regions with $\Delta \log T = 0.04$, which proved adequate. This agrees with the study of Dorman, Irwin, & Pedersen (1991).

For $\log \rho < -6.00$, the gas is very nearly ideal, and the EOS can be computed with a substantially simplified semi-analytic free energy model that includes (1) ideal terms (Maxwell-Boltzmann) and (2) a two-component Debye-Hückel approximation for the weakly coupled plasma interactions. At such low densities, the interactions between neutral particles become negligible and can be safely ignored. Such a simple model can be incorporated as a subroutine in the application code. This approach is preferred for a very low density EOS, as it reduces the need for an extended table and provides higher accuracy than can be obtained by table interpolation.

So far, we have not discussed the contribution of the photon gas to the thermodynamics of the system. The coupling between radiation and matter in thermodynamic equilibrium is very small in the regime where the photon gas contributes significantly to the total pressure (More 1976). This coupling is entirely negligible in the domain defined above, so that the thermodynamics of the photon gas and of the matter can be computed separately and added to obtain a complete EOS. We have thus excluded the photon contribution from our EOS tables although it appears in some of the figures below.

Our EOS code has been constructed to compute the EOS along a single isotherm, proceeding from lower to higher density. For each (ρ, T) point, the code first computes the chemical equilibrium by minimizing the specific (dimensionless) Helmholtz free energy. Since we consider four species in each EOS, and since chemical equilibrium is constrained by the electroneutrality condition and by the definition of the total mass density, the problem is actually reduced to a two-dimensional minimization in concentration space. We perform this minimization using an iterative method due to Powell (Press

et al. 1986, § 10.5). We consider the solution to be converged when the change in the free energy from one iteration to the next is less than one part in 10^9 . Because the free-energy surface has a rather broad minimum, the corresponding accuracy in the concentrations is $\Delta X_i \approx 10^{-7}$.

The pressure and the entropy are next evaluated by differentiating the free energy, holding the concentrations *constant*. Temperature and density differentiations are performed numerically with a simple two-point symmetric scheme using $\Delta\rho/\rho = 10^{-4}$ and $\Delta T/T = 10^{-4}$.

On the other hand, second derivatives of the free energy—which correspond to the first derivatives of P and S —are *not* obtained by differentiation at fixed concentrations. Computing the second derivatives directly from F would require additional free-energy minimizations to “follow” the chemical equilibrium. This was simply impossible to do with the computers available to us. Instead, we have evaluated the second derivatives after the fact by differentiating the pressure and entropy tables as functions of ρ and T . In principle, this method is not as accurate as direct differentiation of F would be if we could perform it. Fortunately, because the second derivatives of the free energy are not all independent, errors arising in the evaluation of these derivatives can be estimated by comparing related quantities directly (see § 8).

5.1. Spline Fitting of the EOS Table

We interpolate in the EOS table with bicubic splines. Differentiating the spline fit of the pressure and entropy surfaces provides a simple way of evaluating the second derivatives of the free energy, with no additional effort.

5.2. Interpolation near the Plasma Phase Transition

Because it is a first-order phase transition, the PPT is characterized by discontinuities in all thermodynamic variables except P , T , and the chemical potentials μ_i . This requires special attention if we wish to have an accurate interpolant near the PPT. We have adopted the following procedure to cope with this problem. We first generate an EOS table covering the range given by equation (23), with the PPT removed by the interpolation method described in § 3.4. We next generate two smaller tables, each with a much finer density grid, by interpolation in the original EOS calculation. These two tables each represent one of the two phases in the regime of pressure ionization (the low- and high-density sides of the PPT), and generous overlap prevents discontinuities with the larger table at the edges. The boundaries of these two tables are

$$3.54 \leq \log T \leq 4.82, \quad (25)$$

with

$$-1.0 \leq \log \rho \leq 0.1 \quad (\text{Phase I}), \quad (26)$$

$$-0.6 \leq \log \rho \leq 0.75 \quad (\text{Phase II}), \quad (27)$$

and grid spacings given by

$$\Delta \log T = 0.08, \quad \Delta \log \rho = 0.025. \quad (28)$$

Thermodynamic quantities for each phase are extrapolated into and beyond the metastable region in order to obtain the rectangular arrays which are used for spline interpolation.

The hydrogen EOS exists in the form of three overlapping tables, as described below, for each of the quantities X_{H_2} , X_{H} , $\log P$, $\log S$, $\log U$ as functions of $\log \rho$ and $\log T$. Given ρ and T , and a knowledge of the coexistence curve (Table 1), which is fitted and stored as a separate equation, it is possible to identify the stable phase of the system and therefore to compute any thermodynamic variable of interest by interpolating in the appropriate table.

5.3. Forms of the EOS Tables

For mixtures of hydrogen and helium, interpolation in composition between the two pure EOS is required. The interpolation scheme we have adopted requires that the independent variables be P and T , instead of the quantities ρ and T which were imposed physically by our choice of the Helmholtz free energy as the basic thermodynamic potential. The transformation of each thermodynamic quantity $W(\log \rho, \log T)$ to $W(\log P, \log T)$ is easily done using one-dimensional spline interpolants along each isotherm. Difficulties arise near the critical point of the PPT, where $\partial P / \partial \rho|_T = 0$. In this region, interpolation into the (P, T) variables can only be approximate. Furthermore, we displaced the critical temperature arbitrarily from the calculated value of $\log T_c = 4.185$ to a tabular value of $\log T_c = 4.18$ so that T_c falls directly on a tabulated isotherm. This small, arbitrary change is well within the uncertainties associated with the PPT (SC2) and dramatically improves the quality of the interpolation.

The final EOS tables with P and T as independent variables cover the following ranges:

$$2.10 \leq \log T \leq 7.06 \quad 4 \leq \log P \leq 19, \quad (29)$$

with $\Delta \log T = 0.08$ and $\Delta \log P = 0.2$. For hydrogen, the two PPT tables cover

$$3.54 \leq \log T \leq 4.82, \quad (30)$$

$$10.5 \leq \log P \leq 12.5 \quad (\text{Phase I}), \quad (31)$$

$$11.6 \leq \log P \leq 14.1 \quad (\text{Phase II}), \quad (32)$$

with grid spacings of $\Delta \log T = 0.08$ and $\Delta \log P = 0.05$.

To summarize, our new equations of state for hydrogen and helium are provided in the form of four tables: one large table each for hydrogen and for helium, in which the regimes of pressure ionization have been artificially smoothed by interpolation, and two small tables (one for each phase) for the hydrogen PPT. The tables are published in the AAS CD-ROM Series, Vol. 5, and a sample is given in Table 2. To minimize interpolation errors, the EOS is tabulated along the same T -grid as the free-energy-minimization calculation. The independent variables are P and T , and the thermodynamic properties of the radiation field are not included. For each $(\log T, \log P)$ entry, we tabulate the following quantities: X_{H_2} , X_{H} (X_{He} and X_{He^+} for the helium EOS), $\log \rho$, $\log S$, $\log U$, $\partial \log \rho / \partial \log$

TABLE 2
SAMPLE HYDROGEN EOS TABLE FOR $\log T = 2.10$

$\log P$ (dyn cm ⁻²)	X_{H_2}	X_{H}	$\log \rho$ (g cm ⁻³)	$\log S$ (erg K ⁻¹ g ⁻¹)	$\log U$ (erg g ⁻¹)	ρ_T^a	ρ_P^a	S_T^a	S_P^a	∇_{ad}
4.00	1.00000E+00	0.00000E+00	-5.7154	8.8910	10.1201	-1.0000	1.0000	0.1687	-0.0530	0.3142
4.20	1.00000E+00	0.00000E+00	-5.5154	8.8803	10.1201	-1.0000	1.0000	0.1729	-0.0543	0.3144
4.40	1.00000E+00	0.00000E+00	-5.3154	8.8693	10.1201	-1.0000	1.0000	0.1773	-0.0557	0.3144
4.60	1.00000E+00	0.00000E+00	-5.1154	8.8580	10.1201	-1.0000	1.0000	0.1820	-0.0572	0.3144
4.80	1.00000E+00	0.00000E+00	-4.9154	8.8464	10.1201	-1.0001	1.0000	0.1869	-0.0588	0.3144
5.00	1.00000E+00	0.00000E+00	-4.7154	8.8345	10.1200	-1.0001	1.0000	0.1921	-0.0604	0.3144
5.20	1.00000E+00	0.00000E+00	-4.5154	8.8222	10.1200	-1.0002	0.9999	0.1976	-0.0621	0.3145
5.40	1.00000E+00	0.00000E+00	-4.3154	8.8096	10.1200	-1.0003	0.9999	0.2034	-0.0640	0.3145
5.60	1.00000E+00	0.00000E+00	-4.1155	8.7966	10.1200	-1.0005	0.9999	0.2096	-0.0659	0.3145
5.80	1.00000E+00	0.00000E+00	-3.9155	8.7832	10.1199	-1.0008	0.9998	0.2162	-0.0680	0.3146
6.00	1.00000E+00	0.00000E+00	-3.7156	8.7694	10.1198	-1.0012	0.9996	0.2233	-0.0703	0.3147
6.20	1.00000E+00	0.00000E+00	-3.5157	8.7551	10.1196	-1.0019	0.9994	0.2309	-0.0727	0.3148
6.40	1.00000E+00	0.00000E+00	-3.3158	8.7403	10.1193	-1.0031	0.9990	0.2392	-0.0753	0.3150
6.60	1.00000E+00	0.00000E+00	-3.1161	8.7250	10.1189	-1.0048	0.9985	0.2482	-0.0782	0.3153
6.80	1.00000E+00	0.00000E+00	-2.9165	8.7090	10.1182	-1.0076	0.9975	0.2581	-0.0815	0.3157
7.00	1.00000E+00	0.00000E+00	-2.7171	8.6923	10.1171	-1.0119	0.9959	0.2693	-0.0852	0.3164
7.20	1.00000E+00	0.00000E+00	-2.5182	8.6749	10.1154	-1.0184	0.9931	0.2821	-0.0895	0.3173
7.40	1.00000E+00	0.00000E+00	-2.3200	8.6565	10.1127	-1.0278	0.9882	0.2973	-0.0948	0.3187
7.60	1.00000E+00	0.00000E+00	-2.1232	8.6369	10.1082	-1.0408	0.9787	0.3159	-0.1013	0.3205
7.80	1.00000E+00	0.00000E+00	-1.9291	8.6158	10.1015	-1.0544	0.9599	0.3394	-0.1094	0.3225
8.00	1.00000E+00	0.00000E+00	-1.7407	8.5930	10.0905	-1.0603	0.9195	0.3686	-0.1189	0.3226
8.20	1.00000E+00	0.00000E+00	-1.5641	8.5683	10.0739	-1.0215	0.8380	0.4052	-0.1282	0.3165
8.40	1.00000E+00	0.00000E+00	-1.4086	8.5421	10.0572	-0.9086	0.7097	0.4370	-0.1325	0.3031
8.60	1.00000E+00	0.00000E+00	-1.2811	8.5157	10.0339	-0.7183	0.5676	0.4532	-0.1308	0.2886
8.80	1.00000E+00	0.00000E+00	-1.1795	8.4897	10.0069	-0.5377	0.4566	0.4803	-0.1302	0.2711
9.00	1.00000E+00	0.00000E+00	-1.0962	8.4634	9.9935	-0.3942	0.3798	0.5104	-0.1335	0.2615
9.20	1.00000E+00	0.00000E+00	-1.0261	8.4361	10.0054	-0.2819	0.3244	0.5271	-0.1389	0.2635
9.40	1.00000E+00	0.00000E+00	-0.9652	8.4078	10.0469	-0.1962	0.2875	0.5173	-0.1440	0.2784
9.60	1.00000E+00	0.00000E+00	-0.9101	8.3787	10.1127	-0.1314	0.2663	0.4937	-0.1473	0.2983
9.80	1.00000E+00	0.00000E+00	-0.8578	8.3490	10.1973	-0.0833	0.2578	0.4751	-0.1494	0.3145

^a See eq. (42).

$T|_P$, $\partial \log \rho / \partial \log P|_T$, $\partial \log S / \partial \log T|_P$, $\partial \log S / \partial \log P|_T$, and the adiabatic gradient, ∇_{ad} . The concentrations X_i are obtained by minimizing the Helmholtz free energy F , and P and S are obtained by numerically differentiating F . The internal energy is obtained from the definition $U \equiv F + TS$, and the derivatives of ρ and S are computed by differentiating bicubic spline fits of the surfaces of $\log \rho$ ($\log T$, $\log P$) and $\log S$ ($\log T$, $\log P$). Other quantities of interest can be obtained from these partial derivatives. Because of the numerical inaccuracies introduced into U by integrating eq. (6), it is preferable to differentiate S rather than U . We use cgs units throughout, with S in ergs g⁻¹ K⁻¹ and U in ergs g⁻¹. The zero point of energy is taken to be that of the ground state of the H₂ molecule for the hydrogen EOS and that of the ground state of the He atom for helium.

The concentrations are defined as

$$X_i = N_i / N, \quad (33)$$

where N is the *total* number of particles, including electrons. With this definition, and considering charge conservation, we have for pure hydrogen

$$X_e = X_{\text{H}^+} = \frac{1}{2}(1 - X_{\text{H}_2} - X_{\text{H}}), \quad (34)$$

and for pure helium

$$X_e = X_{\text{He}^+} + 2X_{\text{He}^{2+}} = \frac{1}{3}(2 - 2X_{\text{He}} - X_{\text{He}^+}). \quad (35)$$

The corresponding number densities n_i of species i are given by

$$n_i = \frac{2\rho / m_{\text{H}}}{1 + 3X_{\text{H}_2} + X_{\text{H}}} X_i \quad (36)$$

for hydrogen species, and

$$n_i = \frac{3\rho / m_{\text{He}}}{1 + 2X_{\text{He}} + X_{\text{He}^+}} X_i \quad (37)$$

for helium species, where $m_{\text{H}} = 1.67357 \times 10^{-24}$ g and $m_{\text{He}} = 6.646442 \times 10^{-24}$ g are the masses of the hydrogen and helium atoms, respectively. As stated in § 5, the concentrations resulting from the free-energy minimization are of limited accuracy.

Moreover, in the interpolation regions of both the H and He EOS the concentrations have very little physical basis but are reasonably well behaved by construction. Therefore, they should not be used when very high accuracy is required, especially when $X_i \ll 1$ for the species of interest. They are provided with the EOS tabulation only because they are required for the calculation of the entropy of mixing discussed in the next section.

6. HYDROGEN AND HELIUM MIXTURES

In most astrophysical problems, hydrogen and helium are not found as pure elements, but are mixed together. It is highly desirable to have an EOS for such mixtures. In practice, it is best to generate a set of tables for H/He mixtures corresponding to a few values for the helium mass fraction $0 \leq Y \leq 1$ and to interpolate between these tables to obtain an EOS for the desired composition. Unfortunately, the complexity of the free-energy model for hydrogen (and of that for helium, if it were comparable in its level of description of the physics) renders such a project unrealistic at this time. A model for a H/He mixture requires a knowledge of the interaction potentials between the various hydrogen and helium species. These are mostly unavailable. In addition, the free-energy minimization would have to be performed in a four-dimensional concentration space, instead of the current two-dimensional cases. This would require an enormous amount of computer time. For the present, the practical solution is to interpolate in composition between the two pure EOS.

Several schemes for interpolation in composition have been discussed and compared by Fontaine et al. (1977). Their study shows that the "additive-volume rule" is superior among those tested. Dorman et al. (1991) also found that it provides satisfactory results, even for interpolation between pure-composition EOS.

The additive-volume rule is based on the fundamental properties of thermodynamic variables. *Intensive* variables, such as the temperature and pressure, must be uniform throughout a system in equilibrium. On the other hand, the volume, entropy, internal energy, etc., are *extensive* variables and are strictly additive for identical systems. This additivity is not valid in general for nonidentical systems, although it is exact in the limit of the ideal, noninteracting gas where no chemical reactions occur. For the fully pressure-ionized gas, numerous simulations have demonstrated the high accuracy of the "linear mixing rule," which is a particular form of the additive-volume rule that holds when the pressure is dominated by the degenerate electron gas (Brami, Hansen, & Joly 1979; Chabrier & Ashcroft 1990). In essence, the additive-volume rule considers the combined system of equations of state for subsystems which are brought into contact, but not allowed to mix microscopically.

Clearly, the additive-volume rule cannot be exact, since it ignores interactions between the helium species and the hydrogen species. Similarly, in an actual mixture, the ionization equilibria of hydrogen and helium are coupled through the electron density. This is not accounted for in the additive-volume rule, and since it cannot predict the correct chemical equilibrium for the mixture, it is not as reliable in regions of partial ionization. These two problems are compounded in the case of

pressure ionization, where mutual interactions are strong. In particular, we expect that the location, the nature, and possibly the very existence of the hydrogen PPT will be affected by the presence of helium. In this particular regime, the additive-volume rule preserves the PPT and its coexistence curve in the (P, T) plane, but it can only be a simple and convenient method at best. Similarly, it is not possible to address the possibility of immiscibility of helium in fully pressure-ionized hydrogen with an EOS interpolated in composition, since the immiscibility arises from the H-He interactions.

For a specific extensive variable W for a combination of subsystems at pressure P and temperature T , the additive-volume rule states that (a derivation is given in Fontaine et al. 1977)

$$W(P, T) = \sum_i X_i W^i(P, T), \quad (38)$$

where X_i is the fraction of the total system occupied by subsystem i . For example, in the case of hydrogen and helium mixtures, the density (which is an inverse specific volume, an extensive quantity) is given by

$$\frac{1}{\rho(P, T)} = \frac{1 - Y}{\rho^{\text{H}}(P, T)} + \frac{Y}{\rho^{\text{He}}(P, T)}, \quad (39)$$

where Y is the helium mass fraction. Similarly, the internal energy per unit mass is given by

$$U(P, T) = (1 - Y)U^{\text{H}}(P, T) + YU^{\text{He}}(P, T). \quad (40)$$

The entropy per gram is interpolated in the same way, except that we supplement the additive-volume rule with a correction for the *ideal* entropy of mixing of the gases. This term is necessary in order to recover the ideal-gas limit, and it is relevant only because the chemical equilibria of the two subsystems are T - and P -dependent. Otherwise, the entropy of mixing would be constant and could simply be ignored. Of course, the true entropy of mixing of H and He must take interactions into account and can only be calculated by solving the full EOS problem for the mixture. In the approximation we have used, we thus write the interpolated entropy as

$$S(P, T) = (1 - Y)S^{\text{H}}(P, T) + YS^{\text{He}}(P, T) + S_{\text{mix}}(P, T). \quad (41)$$

The derivatives of $S(P, T)$ and $\rho(P, T)$ can be obtained by differentiating equations (39) and (41). Using the following notation for the logarithmic derivatives,

$$\rho_T = \left. \frac{\partial \log \rho}{\partial \log T} \right|_P, \quad \rho_P = \left. \frac{\partial \log \rho}{\partial \log P} \right|_T, \quad (42)$$

and with similar definitions for S_T and S_P , we have

$$\rho_T = (1 - Y) \frac{\rho}{\rho^{\text{H}}} \rho_T^{\text{H}} + Y \frac{\rho}{\rho^{\text{He}}} \rho_T^{\text{He}}, \quad (43)$$

$$\rho_P = (1 - Y) \frac{\rho}{\rho^{\text{H}}} \rho_P^{\text{H}} + Y \frac{\rho}{\rho^{\text{He}}} \rho_P^{\text{He}}, \quad (44)$$

$$S_T = (1 - Y) \frac{S}{S_H} S_T^H + Y \frac{S}{S_{He}} S_T^{He} + \frac{S_{\text{mix}}}{S} \left. \frac{\partial \log S_{\text{mix}}}{\partial \log T} \right|_P, \quad (45)$$

$$S_P = (1 - Y) \frac{S}{S_H} S_P^H + Y \frac{S}{S_{He}} S_P^{He} + \frac{S_{\text{mix}}}{S} \left. \frac{\partial \log S_{\text{mix}}}{\partial \log P} \right|_T. \quad (46)$$

Other quantities, such as the adiabatic temperature gradient should not be interpolated using the additive-volume rule; instead they should be obtained from their definition in terms of the quantities given above. For example,

$$\nabla_{\text{ad}} = \left. \frac{\partial \log T}{\partial \log P} \right|_S = - \frac{S_P}{S_T}. \quad (47)$$

The ideal entropy of mixing of m systems each containing N_i particles is

$$S_{\text{mix}}/k_B = N \ln N - \sum_{i=1}^m N_i \ln N_i, \quad (48)$$

where

$$N = \sum_{i=1}^m N_i \quad (49)$$

is the total number of particles. Combining a pure hydrogen subsystem containing \mathcal{N}_H particles (of all hydrogen species, including the “hydrogen” electrons) and a pure helium subsystem of \mathcal{N}_{He} particles, yields the total entropy of mixing as

$$\begin{aligned} \frac{S_{\text{mix}}}{k_B} &= (\mathcal{N}_H + \mathcal{N}_{He}) \ln (\mathcal{N}_H + \mathcal{N}_{He}) - N_{H_2} \ln N_{H_2} \\ &\quad - N_H \ln N_H - N_{H^+} \ln N_{H^+} - N_e \ln N_e - N_{He} \ln N_{He} \\ &\quad - N_{He^+} \ln N_{He^+} - N_{He^{2+}} \ln N_{He^{2+}}. \end{aligned} \quad (50)$$

Here N_e is the *total* number of electrons. However, the entropy of mixing of the various hydrogen species, including the free electrons provided by hydrogen, is naturally taken into account in the H EOS. This is also true of the helium species in the He EOS. Removing these two contributions to the above expression, we find the entropy of mixing which arises only from the mixing of hydrogen and helium,

$$\begin{aligned} \frac{S_{\text{mix}}}{k_B} &= \mathcal{N}_H \ln \left(1 + \frac{\mathcal{N}_{He}}{\mathcal{N}_H} \right) + \mathcal{N}_{He} \ln \left(1 + \frac{\mathcal{N}_H}{\mathcal{N}_{He}} \right) \\ &\quad - N_e \ln N_e + N_e^H \ln N_e^H + N_e^{He} \ln N_e^{He}, \end{aligned} \quad (51)$$

where N_e^H and N_e^{He} are the number of electrons provided by hydrogen and by helium, respectively, and

$$N_e \equiv N_e^H + N_e^{He}. \quad (52)$$

Using the definition of the concentrations and number densities (eqs. [33]–[37]), we obtain the mixing entropy *per gram* in the form

$$\begin{aligned} \frac{S_{\text{mix}}}{k_B} &= \frac{1 - Y}{m_H} \frac{2}{(1 + X_H + 3X_{H_2})} \times \{ \ln(1 + \beta\gamma) \\ &\quad - X_e^H \ln(1 + \delta) + \beta\gamma [\ln(1 + 1/\beta\gamma) \\ &\quad - X_e^{He} \ln(1 + 1/\delta)] \}, \end{aligned} \quad (53)$$

where

$$\beta = \frac{m_H}{m_{He}} \frac{Y}{1 - Y}, \quad (54)$$

$$\gamma = \frac{3(1 + X_H + 3X_{H_2})}{2(1 + 2X_{He} + X_{He^+})}, \quad (55)$$

$$\delta = \frac{3(2 - 2X_{He} - X_{He^+})}{2(1 - X_{H_2} - X_H)} \beta\gamma. \quad (56)$$

The concentrations required to evaluate $S_{\text{mix}}(P, T)$ are tabulated with the EOS. It is straightforward to differentiate $S_{\text{mix}}(P, T)$ as needed for the evaluation of S_T and S_P ; the P and T derivatives of the concentrations X_i can be evaluated numerically from the tables. Figure 3 shows contours of the dimensionless entropy of mixing ($S_{\text{mix}}/k_B/\text{nucleus}$) for $Y = 0.25$, using the H EOS with the PPT. As expected, S_{mix} increases in regions of partial dissociation and ionization and is otherwise constant.

7. THERMODYNAMICS OF HYDROGEN AND HELIUM

The equation-of-state tables for H and He embody a large amount of information which is best visualized with surface plots. In this section, we present the *interpolated* EOS for hydrogen and for helium, with ρ and T as independent variables. The contribution of the photon gas is included in the following figures (but *not* in the EOS tables). These figures show the en-

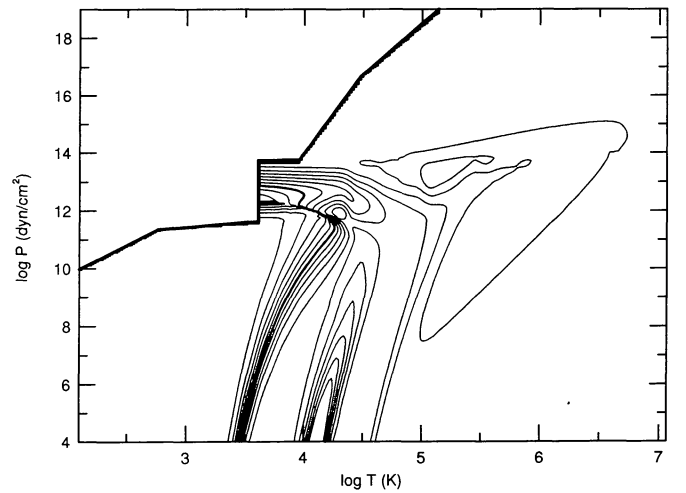


FIG. 3.—Contour plot of the dimensionless entropy of mixing per nucleus, for $Y = 0.25$. The contour levels are separated by 0.005, and the thick curve corresponds to $S_{\text{mix}}/k_B = 0.25$. In the lower left-hand corner of the plot, $S_{\text{mix}}/k_B = 0.222$, and along the $\log T = 7.06$ isotherm, $S_{\text{mix}}/k_B = 0.284$.

tire range of the EOS in these variables and are more easily interpreted in conjunction with the phase diagrams (Figs. 1 and 2).

7.1. Hydrogen

Figure 4 shows the pressure surface. At low temperatures and low densities, hydrogen exists in the form of an ideal gas of H_2 molecules and the pressure is linear in T and ρ . Molecular dissociation and ionization increase the number of particles in the system, causing the two ripples seen at low densities. At high temperatures and low densities, radiation pressure dominates, and P rises as T^4 . At the high-density limit of the figure, the pressure also rises rapidly. At low temperatures, this is caused by the strong repulsive forces between H_2 molecules. For higher temperatures, the EOS calculation for hydrogen reaches the regime of full pressure-ionization, and the pressure is dominated by the electron gas and Coulomb interactions, with $P \propto \rho^{5/3}$ in the limit of complete electron degeneracy.

The entropy (Fig. 5), on the other hand, shows very little variation throughout the whole range covered by our calculation, except for the region where the radiation gas dominates ($S \sim T^3$). The effect of electron degeneracy, which makes an important contribution to the total pressure, is all but invisible in this figure, since the entropy of the electron gas vanishes in the limit of complete degeneracy. Everywhere S increases monotonically as a function of T , ensuring that the specific heat is positive, a fundamental constraint on the EOS. The entropy increases in the regions of dissociation and ionization, where the increasing numbers of particles increases the degree

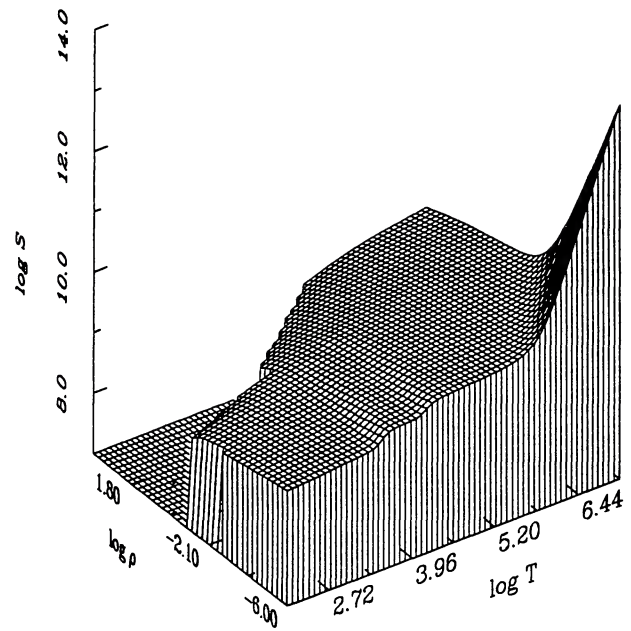


FIG. 5.—Entropy surface for hydrogen. The entropy S is in $\text{ergs g}^{-1} \text{K}^{-1}$.

of disorder of the system. Conversely, S decreases slowly as the density increases, reflecting the gradual ordering of the system. This is not a thermodynamic constraint, but it is generally true in a given phase. Exceptions to this rule are found near phase transitions, and indeed we find $\partial S/\partial \rho|_T > 0$ in a small area centered on the critical point of the PPT (not shown in Fig. 5). It follows from this result and from thermodynamic identities that the thermal expansion coefficient ($\partial P/\partial T|_\rho$) and the adiabatic gradient ∇_{ad} are also negative in this same region.

The internal energy surface shows the same features as the pressure surface, but more clearly (Fig. 6). For ideal H_2 at temperatures well below the characteristic vibration temperature ($\theta_{\text{vib}} = 6100 \text{ K}$), $U = \frac{5}{2}k_B T/m_{H_2}$. On the very lowest isotherms, U drops below this ideal gas value around $\log \rho \approx -1$ (barely visible on the scale of Fig. 6 but see Table 2). This effect originates in the long-range van der Waals attraction between molecules. The depth of this feature decreases rapidly when $k_B T \gg \epsilon$ where ϵ is the depth of the potential well ($\epsilon/k_B = 32 \text{ K}$ for the H_2 - H_2 potential). As the density is increased further, molecules feel the short-range repulsion, and U increases rapidly. As is the case for the entropy, U is increased significantly by dissociation and ionization. This is caused by the increase in the number of particles and by the contribution from the dissociation and ionization energies (which do not appear in S).

In the second-derivative surfaces of the free energy, which are derivatives of the P and S surfaces shown in Figures 4 and 5, respectively, the features we have discussed are greatly amplified. This is also true of any defects in the EOS, such as may arise from flaws in the Helmholtz free-energy model or from numerical inaccuracies in the calculation. In view of the numerous steps involved in our calculations of the second derivatives, we expect them to show some level of numerical noise, as they typically do in this type of EOS work (the EOS of Döp-

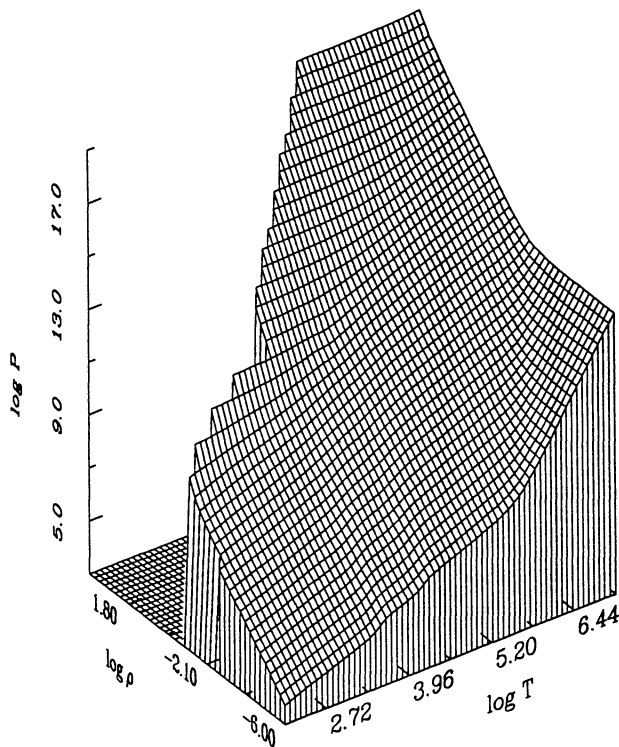


FIG. 4.—Pressure surface for hydrogen. The pressure P is in dyn cm^{-2} .

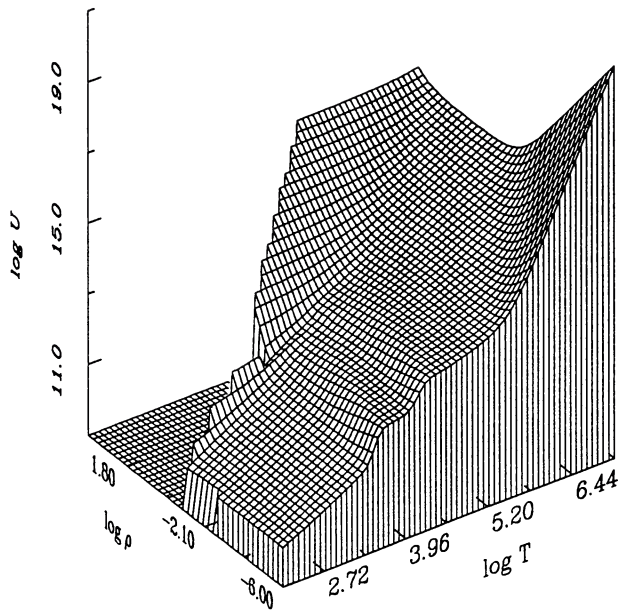


FIG. 6.—Internal energy surface for hydrogen. The internal energy U is in ergs g^{-1} .

pen et al. 1988 is a notable exception, because their model yields analytic expressions for the second derivatives).

Figure 7 shows the logarithmic derivative of the pressure with respect to the temperature, $\chi_T \equiv \partial \log P / \partial \log T|_\rho$. For an ideal gas of particles, $\chi_T = 1$. The two parallel ridges in Figure 7a, at $\log T \approx 3.4$ and $\log T \approx 4.1$ correspond to molecular

dissociation and ionization of hydrogen atoms, respectively. Atomic hydrogen dominates the chemical equilibrium composition in the narrow region in between. The apparent irregularities in these ridges are plotting artifacts. In the high-temperature, low-density region, we have $\chi_T = 4$, the value appropriate to a pure radiation gas. Figure 7b shows the same surface plotted at a different viewing angle. The quantity χ_T drops rapidly with increasing density in the dense molecular fluid because of the strong nonideal behavior of the molecules; the molecular repulsion becomes nearly independent of temperature at high densities, and $\chi_T \rightarrow 0$. A similar behavior is seen at higher temperatures, however, but for a very different reason. In the regime in which hydrogen is fully pressure-ionized, the pressure is dominated by the degenerate electron gas, and P is again independent of T . Some spurious structure is seen between these two regimes, in regions where the EOS was interpolated. In the hydrogen EOS with the PPT, χ_T becomes negative in a small region near the critical point (not shown).

The logarithmic density derivative of the pressure, $\chi_\rho \equiv \partial \log P / \partial \log \rho|_T$ is shown in Figure 8. Mechanical stability of the EOS requires that this quantity, which is a measure of the stiffness of the EOS, be positive. A few limiting regimes are readily identified in this surface. For an ideal gas, we have $\chi_\rho = 1$, and χ_ρ drops to 0 for the photon gas, whose pressure depends only on T . The high- T , high- ρ plateau corresponds to the degenerate electron gas regime, which asymptotically reaches $\chi_\rho = \frac{2}{3}$ in the limit of complete degeneracy. The dramatic rise of χ_ρ with density in the dense molecular regime shows the importance of nonideal effects due to interactions between the molecules. Not only is it necessary to take these effects into account in this part of the phase diagram, but because they come to dominate the contribution of the ideal H_2 fluid, they

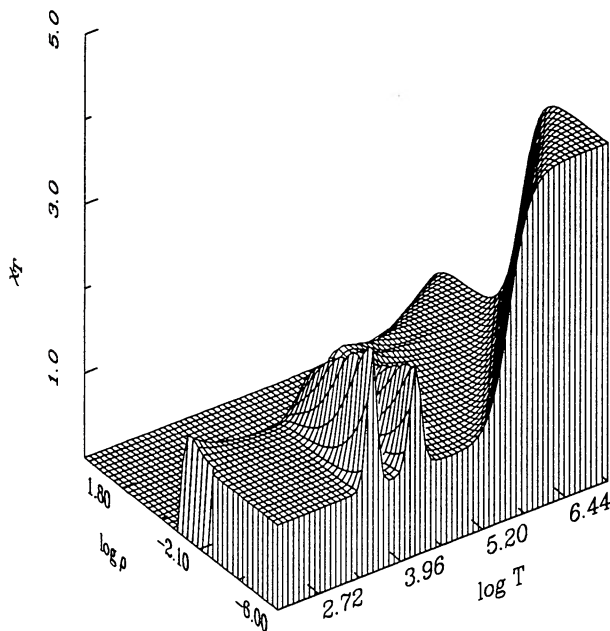


FIG. 7a

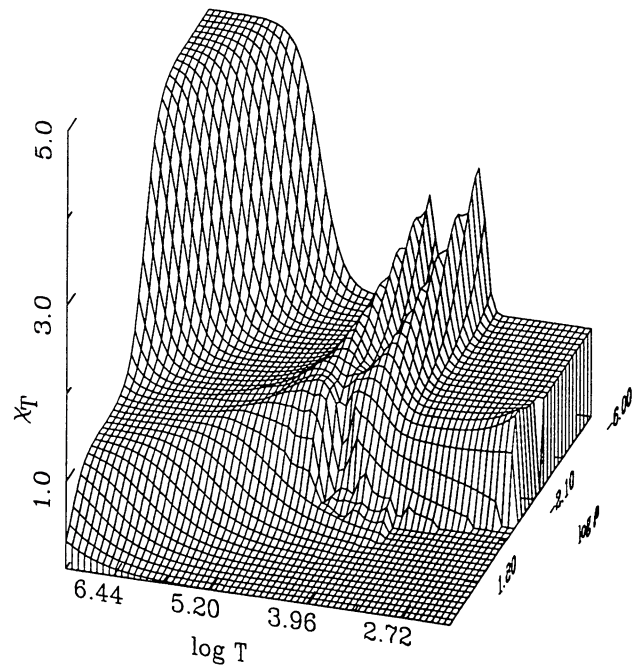


FIG. 7b

FIG. 7.—(a–b) Temperature derivative of the pressure surface for hydrogen, $\chi_T \equiv \partial \log P / \partial \log T|_\rho$, at two different viewing angles

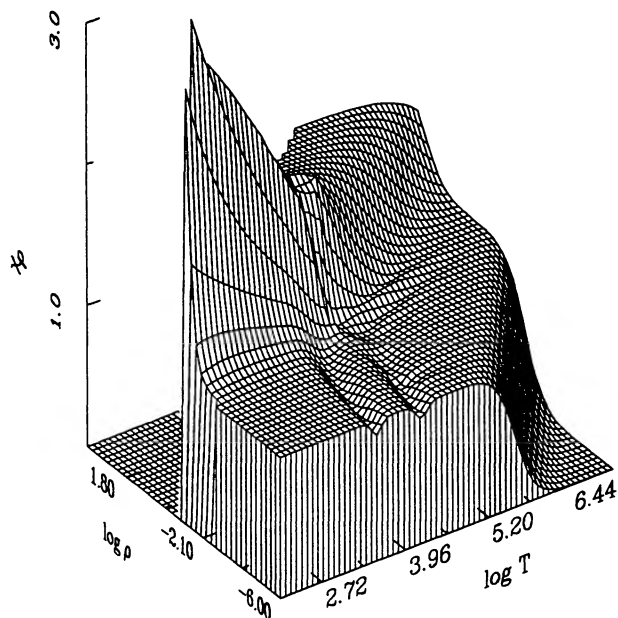


FIG. 8.—Density derivative of the pressure surface for hydrogen, $\chi_\rho \equiv \partial \log P / \partial \log \rho|_T$.

must be modeled in a realistic fashion. Two shallow valleys again display changes in the chemical equilibrium of the system as T is increased. The effect is not as large in χ_ρ as in χ_T , since temperature dissociation and ionization depend mostly on T and not ρ , as can be understood from the slopes of the dashed lines in Figure 1. Were these lines vertical in the phase diagram, the two valleys in Figure 8 would vanish. The interpolation region again shows non-physical structure. In the EOS with the PPT, we find $\chi_\rho = 0$ identically at the critical point, as is required by definition.

The specific heat at constant pressure, C_p , is shown in Figure 9. The fundamental thermodynamic constraints of stability of the EOS require that $C_p > 0$ everywhere. In terms of the independent variables ρ and T , C_p is a function of three partial derivatives of the free energy:

$$C_p = T \left. \frac{\partial S}{\partial T} \right|_p = T \left. \frac{\partial S}{\partial T} \right|_\rho + \frac{P \chi_T^2}{\rho T \chi_\rho}. \quad (57)$$

Since each second-derivative surface carries its own flaws and spurious features, the specific heat at constant pressure, which combines three of them, is particularly sensitive to these inaccuracies. The specific heat of the ideal gas (low density) increases as the fluid becomes successively molecular (H_2), atomic (H), and finally fully ionized (H^+ and e). Because of (1) the increase in the number density of particles and (2) the substantial energy involved in the dissociation of the molecule and the subsequent ionization of the atom, the specific heat reaches local maxima in the partial dissociation and ionization zones. For a pure photon gas, C_p diverges, and the very rapid rise seen at high temperatures reflects the diminishing contribution of matter to the EOS. The irregular depression in Figure 9 corresponds to the interpolation region of the hydrogen EOS,

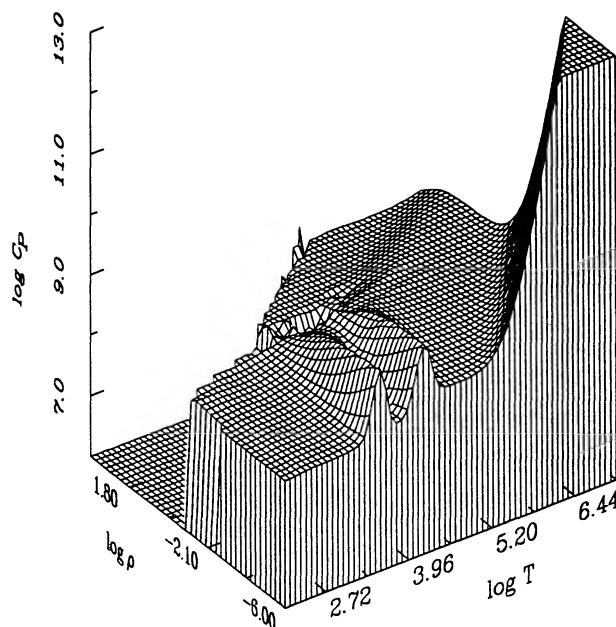


FIG. 9.—Surface of the specific heat at constant pressure for hydrogen, in $\text{ergs g}^{-1} \text{K}^{-1}$. The rapidly rising peak is arbitrarily truncated at $\log C_p = 13$ for scaling purposes.

where a variety of flaws combine. In this region, C_p is rather inaccurate. The irregular behavior of the specific heat along the high-density edge of the table is caused by difficulties in interpolating and differentiating at the table boundary.

We display the adiabatic temperature gradient in Figure 10. This quantity plays a central role in theories of convection and

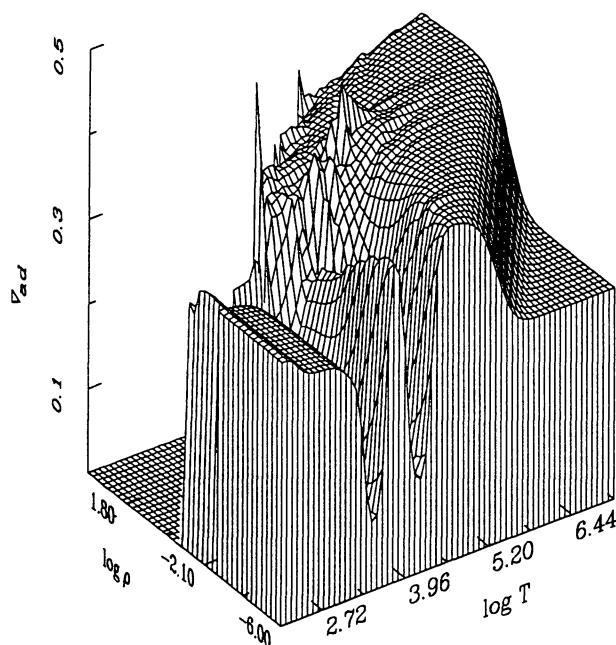


FIG. 10.—The adiabatic gradient surface for hydrogen, $\nabla_{\text{ad}} \equiv \partial \log T / \partial \log P|_S$.

pulsation. In terms of the independent variables ρ and T , we have

$$\nabla_{\text{ad}} = \left. \frac{\partial \log T}{\partial \log P} \right|_S = \chi_T - \frac{\rho S T \chi_\rho}{P \chi_T} \left. \frac{\partial \log S}{\partial \log T} \right|_P; \quad (58)$$

this expression also involves three second derivatives of the free energy. As a consequence, we expect ∇_{ad} to be noisier than the first derivatives of S and P . A number of familiar features are readily identified in this surface. The adiabatic gradient of an ideal monatomic gas is 0.4, a value approximated by the low-density plasma and nearly reached in the narrow region dominated by atomic hydrogen. Molecular dissociation and temperature ionization carve two deep “valleys” in the ∇_{ad} surface. Such dramatic drops in the value of the adiabatic gradient greatly favor the onset of convection in stars. For a pure photon gas, we have $\nabla_{\text{ad}} = 0.25$, which is the value of the high-temperature, low-density plateau in Figure 10. Because of the internal structure of H_2 , $\nabla_{\text{ad}} \neq 0.4$ for the ideal molecular fluid. The rotation temperature of H_2 is $\theta_{\text{rot}} = 85$ K and not all rotational levels are populated at the low-temperature end of Figure 10. As T increases, ∇_{ad} decreases to $\frac{2}{7} \approx 0.286$, the value for a classical, rigid rotating molecule with 2 degrees of rotational freedom and 3 degrees of translational freedom. This situation is realized when $T \gg \theta_{\text{rot}}$, but with $T \ll \theta_{\text{vib}}$. At low densities, molecular dissociation occurs before significant vibrational excitation takes place. The adiabatic temperature gradient surface is rather rugged in the interpolation region, with large, unphysical excursions from the surrounding smooth surface. A few large peaks are also found at the high-density edge of the figure. They are caused by edge effects in the interpolation/differentiation of the S and P surfaces.

The irregularities in the EOS surfaces are most obviously present in the interpolated region. They are partly caused by the fact that we have interpolated along isotherms, and therefore the temperature derivatives of S and P are not as smooth as the density derivatives. Some of the problems seen in C_p and ∇_{ad} arise from our separate interpolation of the entropy and of the pressure, which introduces thermodynamic inconsistency into the EOS (see § 8 below).

In § 9, where we compare our H EOS with other equations of state, we discuss some of the features described above in more quantitative detail.

7.2. Helium

The He EOS surfaces are shown in Figures 11–17. They are qualitatively very similar to the corresponding figures for hydrogen. The main differences are

1. Helium does not form molecules and has a high first-excitation energy. It behaves very much like a monatomic fluid without internal structure up to temperatures where ionization begins ($\log T \approx 4.1$).

2. While there is no molecular dissociation region for He, temperature ionization occurs in two stages, first to He^+ and then to He^{2+} . These two ionization zones are more closely spaced in temperature than are the dissociation and ionization zones of hydrogen.

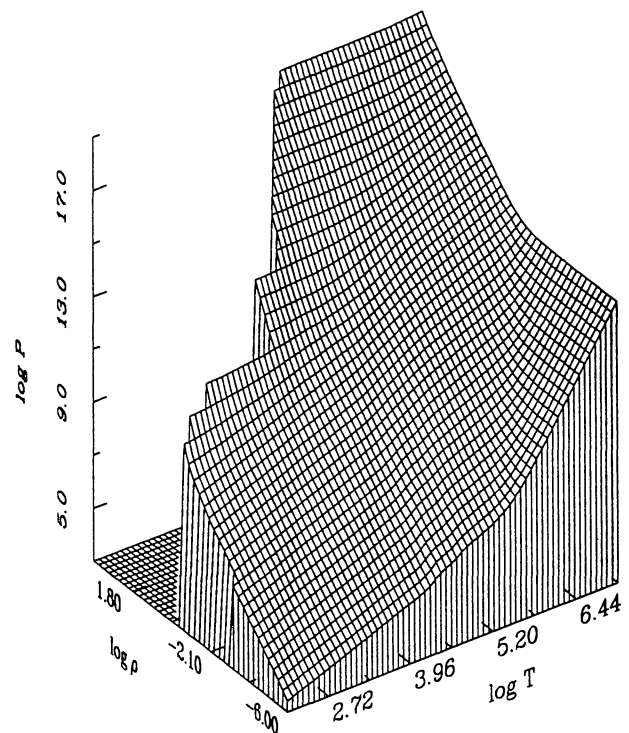


FIG. 11.—Pressure surface for helium. The pressure P is in dyn cm^{-2} .

3. The atomic He fluid does not interact as strongly as the molecular H_2 fluid.

4. Coulomb forces are stronger in the fully ionized He plasma due to the higher charge of the ions.

Figures 11–13 show the surfaces for the pressure, entropy, and internal energy, respectively. Physical regimes similar to

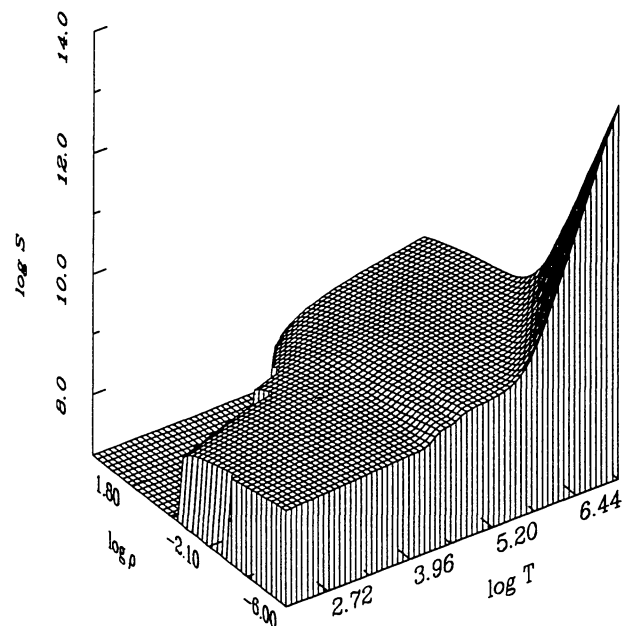


FIG. 12.—Entropy surface for helium. The entropy S is in $\text{ergs g}^{-1} \text{K}^{-1}$.

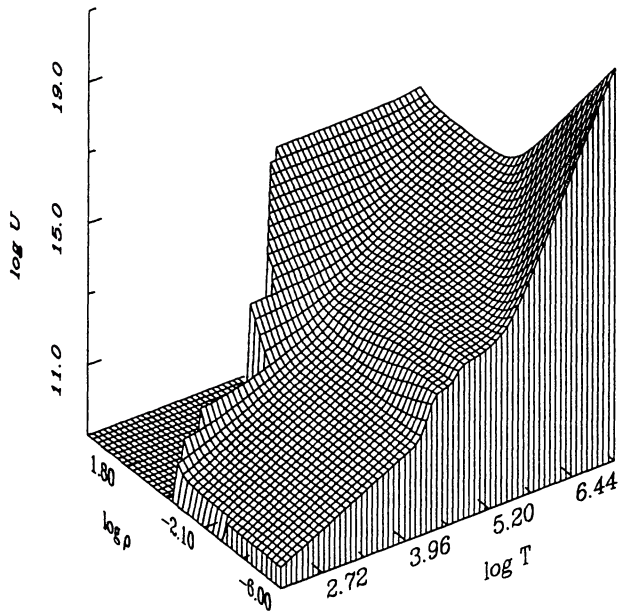


FIG. 13.—Internal energy surface for helium. The internal energy U is in ergs g^{-1} .

those discussed above for hydrogen can also be identified on these figures.

Figure 14 shows χ_T . It remains close to the ideal-gas value $\chi_T = 1$ over a much wider range in temperature and density than is the case for hydrogen, due to the effectively structureless and monatomic nature of the He fluid. Two well-defined ridges correspond to the two ionization stages of helium. The bumps

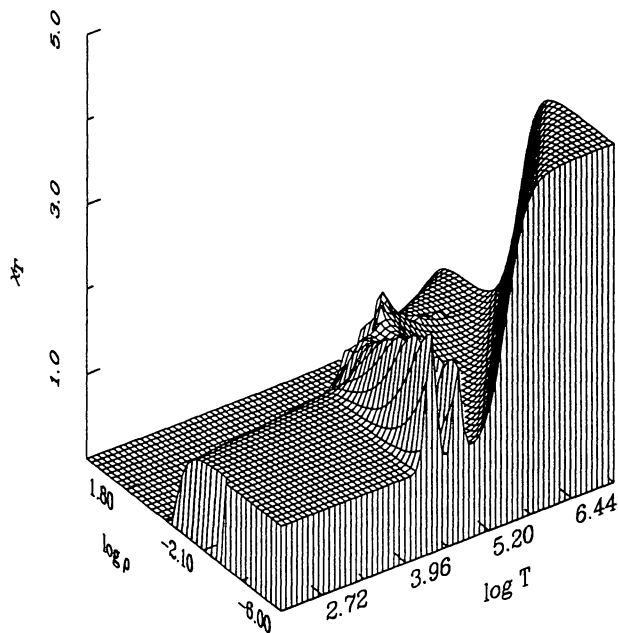


FIG. 14a

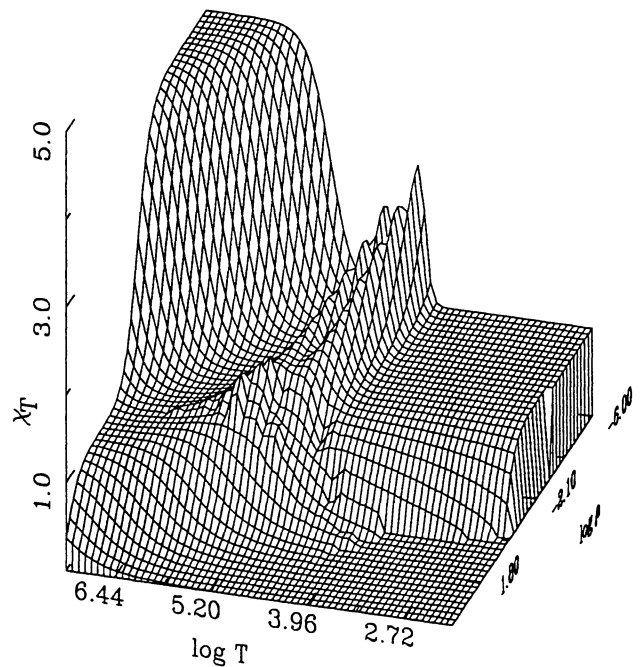


FIG. 14b

FIG. 14.—(a–b) Temperature derivative of the pressure surface for helium, $\chi_T = \partial \log P / \partial \log T|_p$, under two different viewing angles

on the crests of these ridges are plotting artifacts. Figure 14b shows the same surface from a different viewing angle, emphasizing the high-density behavior of χ_T . The rapid decreases in χ_T at low T resulting from the He-He interactions and at high T resulting from electron degeneracy are readily apparent. The irregular structure apparent in the intermediate regime again corresponds to the interpolation region and has no physical basis.

The χ_p surface for He (Fig. 15) is very similar to that for H (Fig. 8). The He-He repulsion in the dense atomic fluid phase is not as strong as the $\text{H}_2\text{-H}_2$ repulsion; this is reflected in the lower values of χ_p for He in this regime. The asymptotic value $\chi_p = \frac{5}{3}$ for the very dense, fully ionized plasma dominated by electron degeneracy pressure is reached at higher densities than in the case for hydrogen because of the stronger Coulomb interaction between the doubly charged He^{2+} ions. While some irregular behavior is noticeable in the interpolation region, the χ_p surface is generally rather smooth.

The specific heat at constant pressure (Fig. 16) is also quite smooth, even in the interpolation region, where there is a depression in C_p . This depression is probably not real. This feature is not nearly as deep as in the case of hydrogen (Fig. 9), because of the wider density range used for the He EOS interpolation.

Three spurious large-amplitude peaks in the adiabatic gradient surface (Fig. 17) result from edge effects in interpolation/differentiation of the P and S surfaces and have no physical basis.

8. THERMODYNAMIC CONSISTENCY

The preceding discussion demonstrates that the second derivatives of the free energy are very sensitive to the details of

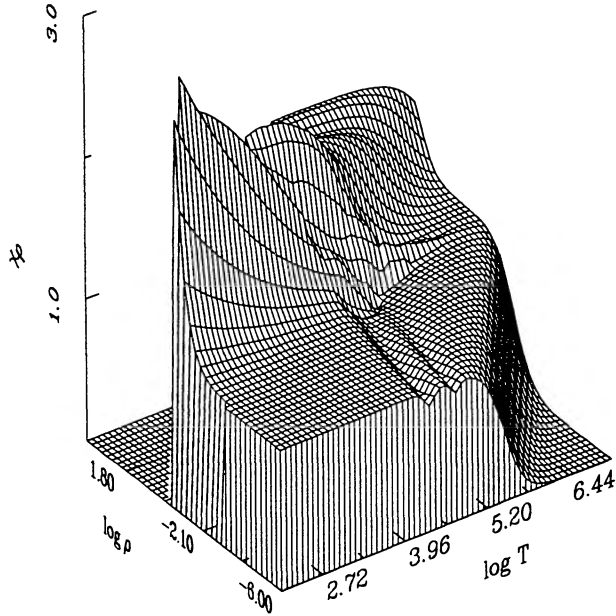


FIG. 15.—Density derivative of the pressure surface for helium, $\chi_\rho = \partial \log P / \partial \log \rho|_T$.

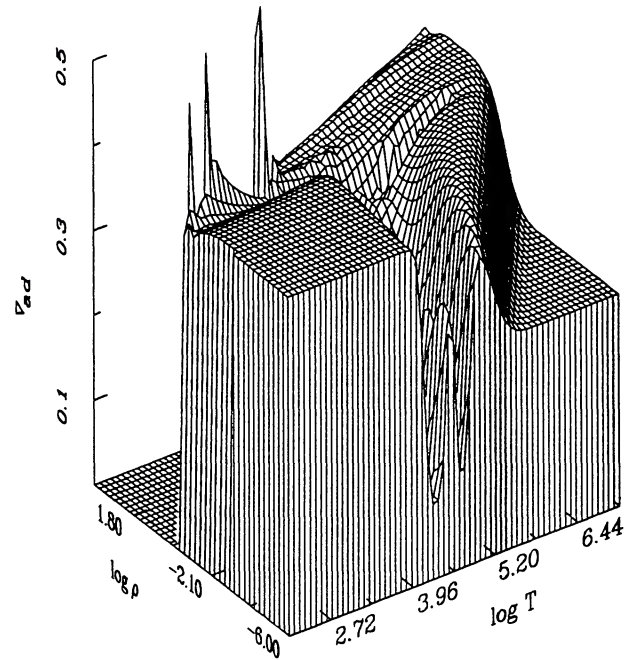


FIG. 17.—Adiabatic gradient surface for helium, $\nabla_{\text{ad}} = \partial \log T / \partial \log P|_S$.

the EOS calculation and are apt to reveal flaws at a glance. An even more sensitive test of an EOS is thermodynamic consistency, which—like the fundamental constraints of stability of the EOS—is a necessary but not sufficient condition to ensure accuracy. Since all equilibrium thermodynamic quantities are obtained by taking derivatives of a single function, the Helmholtz free energy F , the quantities which correspond to mixed

partial derivatives of F are related. The well-known Maxwell relations follow from this fact. If some region of the EOS does not satisfy the Maxwell relations, it is said to be thermodynamically inconsistent in this region. For the quantities of interest here, and with our choice of P and T as independent variables, the Maxwell relation of principal interest is

$$\left. \frac{\partial S}{\partial P} \right|_{T, \{N_j\}} = - \left. \frac{\partial V}{\partial T} \right|_{P, \{N_j\}}. \quad (59)$$

In terms of the mass density ρ , and defining \tilde{S} as the entropy per unit mass, we obtain

$$\left. \frac{\partial \rho}{\partial T} \right|_P = \rho^2 \left. \frac{\partial \tilde{S}}{\partial P} \right|_T. \quad (60)$$

It can be shown that the particle numbers of each species N_j need not be held constant when taking the derivatives in eq. (60) if they are at their chemical equilibrium values for all P and T . We thus define the following index,

$$\alpha = \frac{1}{\rho^2} \left. \frac{\partial \rho}{\partial T} \right|_P \left(\left. \frac{\partial \tilde{S}}{\partial P} \right|_T \right)^{-1} - 1, \quad (61)$$

which vanishes where the EOS is thermodynamically consistent.

In Figure 18, contours of α are shown for the interpolated hydrogen EOS. The boundaries of the interpolation region are indicated by the heavy solid lines forming an irregular box centered on $\log T \approx 4$ and $\log P \approx 13$. The contours are plotted at the following levels: $\alpha = (\pm)0.01, 0.032, 0.1, 0.316$, and 1, with

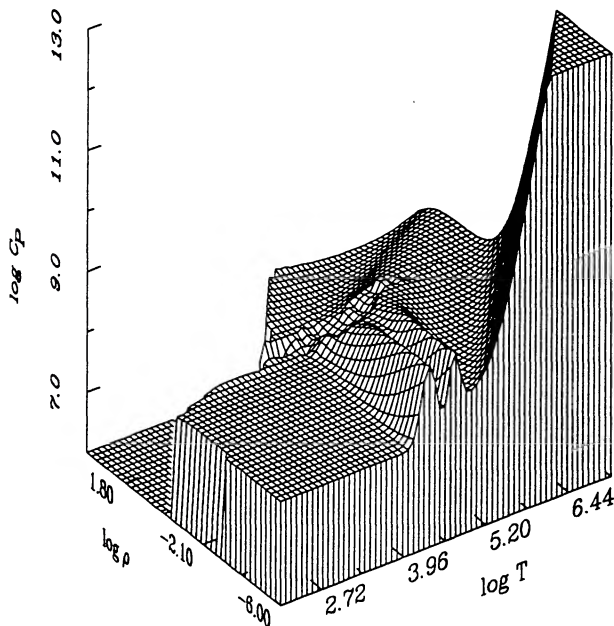


FIG. 16.—Surface of the specific heat at constant pressure for helium, in $\text{ergs g}^{-1} \text{K}^{-1}$. The rapidly rising peak is arbitrarily truncated at $\log C_p = 13$ for scaling purposes.

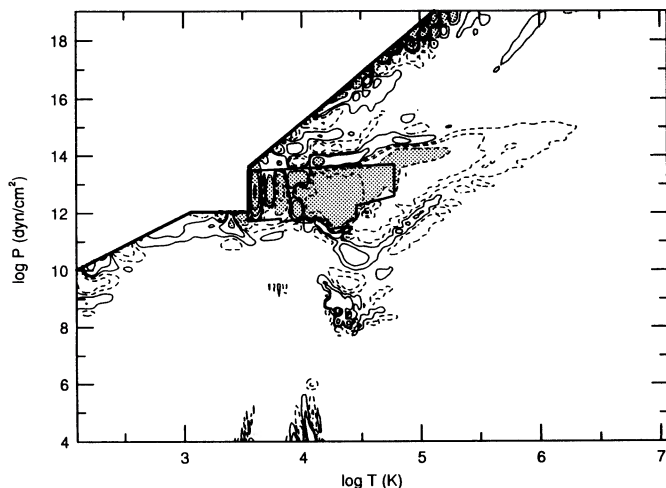


FIG. 18.—Contours of the thermodynamic consistency index α (eq. [61]) over the entire *interpolated* hydrogen EOS table. Positive and negative contours are represented by solid and dashed lines, respectively. The contour levels are $(\pm) 0.01, 0.032, 0.1, 0.316$, and 1 , i.e., they are separated by 0.5 dex. Shaded areas correspond to $|\alpha| \geq 0.1$. See text.

negative values indicated by dashed contours. The shaded area corresponds to $|\alpha| \geq 0.1$. This figure covers the entire (P, T) range of the EOS.

A number of features are immediately apparent. For $\log P < 10$, thermodynamic inconsistency up to the 3%–5% level is associated with the temperature dissociation and ionization zones. As discussed above, P and S vary rapidly with temperature over these narrow zones. While the P and S surfaces may be completely thermodynamically consistent with each other, the bicubic spline interpolant does not necessarily estimate the derivatives accurately (in this case, $\partial\rho/\partial T|_P$), introducing oscillations in α . Adding isotherms to the EOS table with a spacing of $\Delta \log T = 0.04$ improved the accuracy of the spline fitting remarkably but more are needed to remove this blemish entirely. This also indicates that an isotherm spacing of no more than $\Delta \log T = 0.04$ is necessary for accurate differentiation of the EOS in the partial ionization zones. Along the high-pressure boundary of the table, consistency is not very good, with α usually below 10%, but with a few isolated peaks up to 30%. This is clearly due to an edge effect in the spline interpolation, made even more apparent by the cellular pattern in the contours at the highest pressures. This cell size corresponds to the grid size in the EOS computation in the (ρ, T) plane. Finally, the worst departures from thermodynamic consistency are found in the interpolated region. This was anticipated from the fact that P and S were interpolated separately and is obvious from the relation between the contour pattern and the boundaries of the extrapolated region. The signature of the $\Delta \log T = 0.08$ spacing of the isotherms is also clear. Attempts to decrease $|\alpha|$ by adjusting the interpolated surfaces locally proved unsuccessful.

Figure 19 shows the contours of α near the PPT of hydrogen on an expanded scale. The coexistence curve of the PPT is shown by the heavy solid curve. The features away from the PPT are identical to those of Figure 18, since both hydrogen EOS are the same outside the interpolation region. Just below

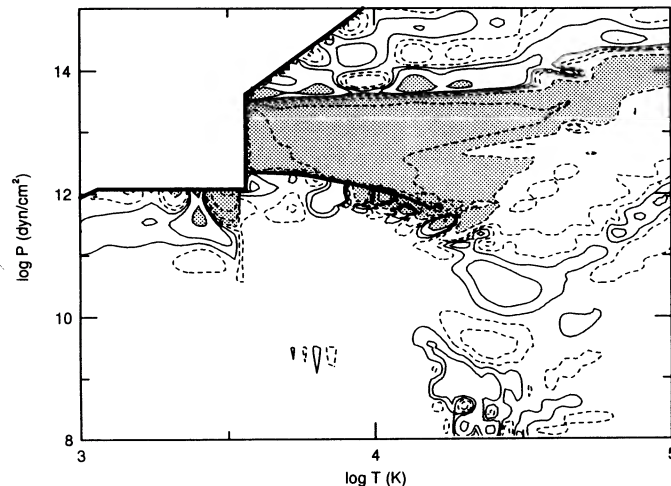


FIG. 19.—Contours of the thermodynamic consistency index α around the plasma phase transition of the hydrogen EOS. The coexistence curve of the PPT is shown by the heavy solid curve. See caption for Fig. 18.

the PPT the effect of grid spacing is obvious in the cellular pattern of the contours. A finer T -grid would be desirable in this region. Above the PPT, severe departures from thermodynamic consistency are found. Even if the FMIN method guarantees thermodynamic consistency in principle, violations can arise in two ways: (1) the steps $\Delta\rho$ and ΔT used to differentiate F to get P and S , respectively, can become too large near the PPT for an accurate calculation of P and S , and (2) the bicubic spline interpolant is ill behaved near the PPT, and it leads to poor values for the second derivatives of F . On the other hand, the extended ridge between $\log P \approx 13.0$ and 13.5 is caused by the second interpolation performed to remove the discontinuous and unphysical behavior of the EOS in this regime (see § 3.3.1). In this case, it is $\partial S/\partial\rho|_T$ which is erroneous.

The departures from thermodynamic consistency in the helium EOS (Fig. 20) share similarities with the case of hydrogen.

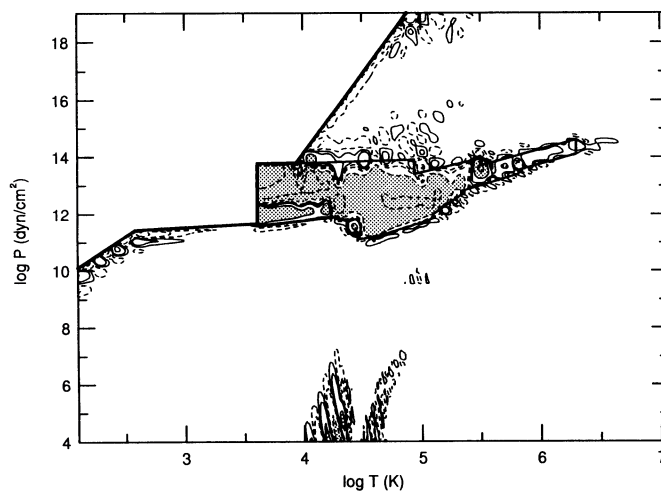


FIG. 20.—Contours of the thermodynamic consistency index α over the entire (interpolated) helium EOS table. See caption for Fig. 18.

The interpolation region for the He EOS is outlined with a heavy solid line. The interpolation region for He is more extensive than that for hydrogen because of the limitations of the low-density model we have used for the Helmholtz free energy of He (§ 4.2). Except for a few isolated regions, thermodynamic consistency to within a few percent is achieved for both the hydrogen and the helium EOS. While the FMIN method guarantees thermodynamic consistency in principle, numerical errors creep in at various stages of the calculation, particularly in the evaluation of the derivatives of S and P with a spline interpolant. These can be removed by computing the EOS on a finer grid. The largest departures from thermodynamic consistency typically occur in the interpolated regions of the EOS, as anticipated. This is caused by our decision to reduce the density range of the interpolation as much as possible and by interpolating P and S separately. This improves the accuracy of S and P separately, but at the cost of thermodynamic consistency.

9. COMPARISON WITH OTHER HYDROGEN EOS

Except for analytic calculations valid only over limited regimes of ρ and T , most EOS calculations involve a large number of approximations and assumptions as well as some level of internal inconsistency, as exemplified by the above discussion. This makes it difficult both to judge which of the available EOS is the most appropriate for a given astrophysical problem and also to assess its degree of reliability. It is usually very difficult to answer such questions from the published literature alone. A direct, numerical comparison among different EOS tables, computed with different underlying assumptions, is essential to reveal flaws and poor approximations and to develop a healthy appreciation of the uncertainties that persist in some physical regimes. This section is devoted to a comparison of the present hydrogen EOS with other equations of state often used in astrophysics.

In the spirit of clarity and conciseness, the comparison we have performed is limited to five hydrogen equations of state: the table of Fontaine et al. (1977); the pure H case of the H/He EOS of Magni & Mazzitelli⁸ (1979); a pure hydrogen calculation based on the model developed by Mihalas, Hummer, & Däppen (Däppen et al. 1988 and references therein); the SESAME library material 5251 EOS, developed at the Los Alamos National Laboratory (Kerley 1972); and the present EOS. Hereafter, these five equations of state are denoted by FGVH, MM, MHD, LANL, and SC, respectively.

These EOS span over 20 years of effort in developing reliable EOS for stellar envelopes and interiors, and they are representative of the better EOS currently in use. Except for the SC EOS, they have been used extensively in a variety of astrophysical contexts (see Chabrier et al. 1992, however). While they have a number of features in common, they differ greatly in detail, in the level of statistical mechanical consistency of the model, and in the accuracy of the modeled contributions to the free energy.

The LANL EOS is actually a deuterium EOS scaled in density. Most contributions to the free energy of deuterium scale

exactly in density but the procedure is not appropriate in the molecular phase. The energy levels of the molecule depend upon the moment of inertia and the reduced mass of D_2 which are twice as large as for H_2 . While this does not affect the pressure in the molecular phase, the internal energy of the LANL EOS is overestimated by up to 6% for $\log T \lesssim 3.3$ (Saumon & Van Horn 1987).

9.1. EOS Comparison along Isotherms

To minimize spurious errors, we have avoided numerical interpolation in the tables as much as possible. To this end, we selected six isotherms common to four EOS: $\log T = 3.70, 4.10, 4.50, 5.30, 6.10,$ and 6.90 . The last three isotherms are not tabulated by MM, and we performed the necessary temperature interpolation using a program provided with their table. The LANL EOS has no isotherm in common with the other four EOS, so we interpolated it linearly in $\log T$. The figures below show the density points of the original tables connected by straight lines; the EOS were not “smoothed.” However, it has been noted before that the FGVH EOS has a number of “bad points” at which the second derivatives of the free energy show anomalous behavior. Since these points are isolated, they must arise not from deficiencies in the underlying thermodynamic description but instead from some localized numerical quirk. A few of these points are found in the six isotherms under consideration, and we corrected the discordant values by a simple interpolation in density. These points are located at $(\log T, \log \rho)$: $(4.10, -5.667), (4.50, -3.667), (5.30, -2.333)$ for ∇_{ad} .

The quantities we have compared are $\log P$, $\log U$ and ∇_{ad} for all six isotherms. Exceptions to this rule are the MHD EOS, which has no points at $\log T = 6.10$ and 6.90 , because the table supplied to us is limited to $\log T \leq 6$, and the MM EOS, which tabulates only $\log P$, ∇_{ad} , and C_p , the specific heat. This last quantity is not used in the present comparison. The LANL EOS tables available to us provide only P and U . The second derivatives were not generated from these tables to avoid introducing spurious differentiation and interpolation errors. Note that all quantities shown here are taken directly from the EOS tables and are not constructed from other quantities by using thermodynamic identities, for example. This avoids introducing potential errors due to thermodynamic inconsistency in the EOS or numerical inaccuracies in the procedure. In all four cases, the zero of energy is chosen as the ground state of the H_2 molecule and the contribution of the photon gas is included.

The four EOS are compared in Figures 21–23, and it is readily apparent that the differences can be substantial. As a point of reference, for the SC EOS the quantities P and U are within 1% of their ideal gas value for $\log \rho < -2$. It is easy to verify that the nonideal terms are very small at such low densities simply by comparing the volume occupied by atoms (or molecules) to the total volume. Surprisingly, significant differences with some of the other EOS are found even for densities below $\log \rho = -2$.

9.1.1. The Pressure

Figure 21a shows the pressure for four EOS along the six isotherms. At densities above and below the range shown in this figure, the agreement is satisfactory. The hottest two isotherms correspond to a fully ionized gas of H^+ and e interact-

⁸ Our study of the MM EOS table which we obtained in 1987 shows that it is much improved over the version published in Magni & Mazzitelli (1979).

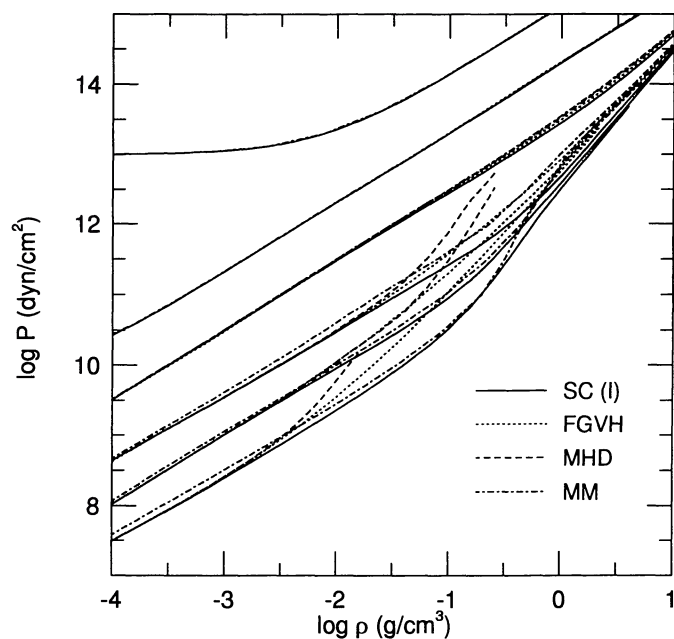


FIG. 21a

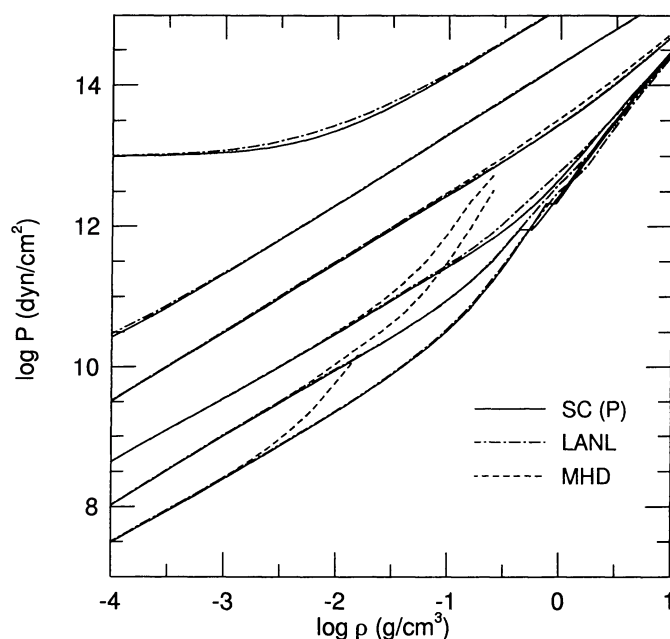


FIG. 21b

FIG. 21.—Comparison of pressure isotherms. (a) the SC(I) (interpolated), FGVH, MHD, and MM equations of state. (b) The SC(P) (with PPT), LANL, and MHD equations of state. The isotherms are (from top to bottom): $\log T = 6.90, 6.10, 5.30, 4.50, 4.10,$ and 3.70 .

ing weakly in the Debye-Hückel limit. The photon pressure dominates gas pressure when P becomes independent of ρ along the $\log T = 6.90$ curve. The agreement is excellent in this relatively simple regime but severe divergences are found at lower temperatures. Curiously, the MM EOS systematically overestimates P at low densities, where the gas is ideal for all practical purposes. This is most likely due to an overestimate of the degree of dissociation and perhaps ionization which arises from their treatment of the IPF of H and of H_2 .⁹

For the lowest three isotherms, the MHD and FGVH EOS predict much higher pressures than either the SC or the MM EOS at moderate densities. The high pressures of FGVH and MHD are caused by the hard sphere potential they used to model the interactions between neutral particles. This potential qualitatively models the strongly repulsive cores of the actual potentials, but being infinitely repulsive, it fails to describe adequately the softness of the repulsion. This feature of neutral-neutral interactions becomes important at high densities. The hard sphere potential is too repulsive at high densities and leads to overestimated pressures even in a regime where the gas should be nearly ideal. The authors of the MHD EOS point out that their EOS should not be used for $\log \rho > -2$, a safe limit at low T in view of the above observation.

In the regime of pressure ionization ($-0.5 < \log \rho < 0.5$), the SC, MM, and FGVH EOS can differ by up to a factor of 2 in P . In all three cases, thermodynamic quantities were smoothly interpolated between a low-density and a high-density regime where the authors felt that their respective EOS were reliable.

In Figure 21b, we compare the SC EOS (with the PPT),

⁹ Their IPF for H_2 has been corrected since we obtained the MM table in 1987 (Mazzitelli 1993).

LANL, and MHD, the latter being common to both Figures 21a and 21b. This comparison shows that the LANL EOS agrees quite well with the SC EOS, the PPT being revealed by the density discontinuity on each of the lowest two isotherms. Breaks in the lowest two LANL curves are similarly due to a transition to a metallic solid hydrogen phase, although the transition itself is not explicitly plotted here, unlike the SC(P) case. This is qualitatively different from the PPT of SC, since the SC EOS predicts that metallic hydrogen is in a fluid state above the PPT.

9.1.2. Internal Energy

Most of the features discussed above can also be seen in the internal energy U , shown in Figure 22. Again, we see that for $\log T < 4.50$ and $\log \rho > -2$, the hard-sphere model used by FGVH and MHD leads to an overestimate of U (Fig. 22a). The $\log \rho = -2$ limit recommended by MHD is a sensible choice for U as well as for P .

The two intermediate isotherms illustrate the importance of careful treatment of the influence of neighboring particles on the IPF. For the $\log T = 4.50$ isotherm, SC lies above MHD, while the reverse is true for $\log T = 5.30$. At these low densities, characteristic of the ideal gas, this arises from differences in the degree of ionization, which is directly affected by the IPF of atomic hydrogen. At these temperatures, thermal excitation of H becomes significant and the chemical equilibrium depends on the number of states retained in the IPF sum.¹⁰ This effect

¹⁰ The SC and MHD EOS do not use a cutoff in the IPF sum but instead remove the bound states gradually, following the "occupation-probability" formalism presented in Hummer & Mihalas (1988). It is nevertheless useful to think in terms of a sharp cutoff in the present context.

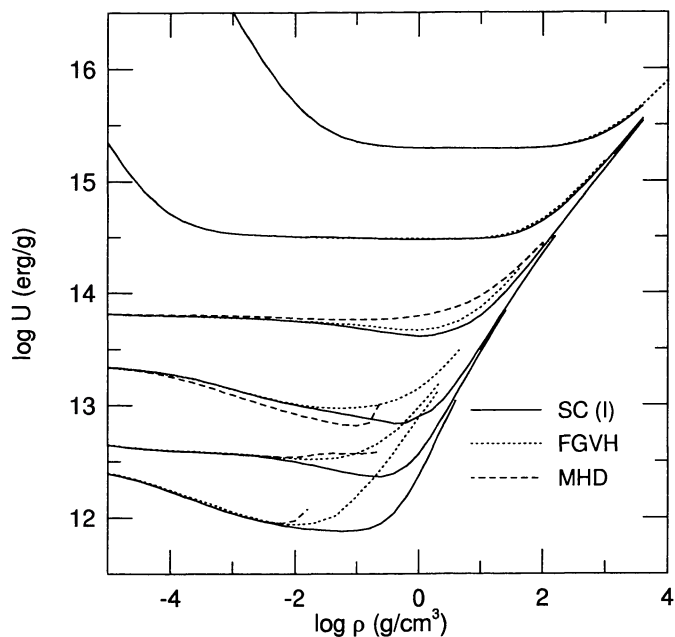


FIG. 22a

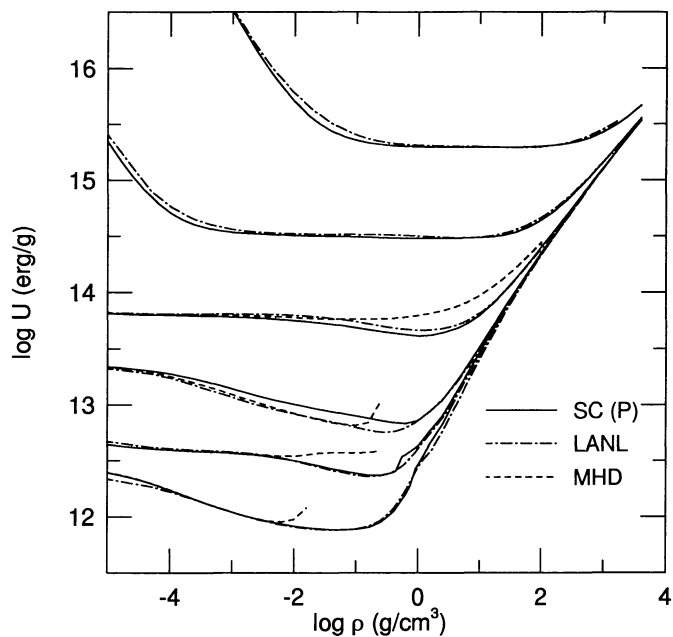


FIG. 22b

FIG. 22.—Comparison of internal energy isotherms. (a) SC(I) (interpolated), FGVH, and MHD equations of state. (b) SC(P) (with PPT), LANL, and MHD equations of state. The isotherms are (from top to bottom): $\log T = 6.90, 6.10, 5.30, 4.50, 4.10,$ and 3.70 .

is not visible in the pressure because it is relatively insensitive to the excitation energies of bound species.

At $\log T = 4.50$, the degree of ionization is sufficiently low for the finite “sizes” of atoms to provide the main nonideal contribution. This, in effect, is an “excluded volume” interaction, which removes the upper levels of the IPF to ensure that the atoms do not “overlap.” MHD adopted a fixed and somewhat arbitrary diameter for the H atom in its ground state (1.06 Å) while SC use a thermodynamic criterion (SC1) to compute a temperature- and density-dependent value ranging from 1.1 to ~ 1.6 Å. Fewer states are retained in the IPF when the hard-sphere diameter is larger, favoring a higher degree of ionization in the SC EOS and a larger U . Because the SC EOS uses more realistic interaction potentials between neutral particles and a thermodynamic criterion to obtain the hard sphere diameters of H and H₂, we believe that it is more reliable in this regime than the MHD EOS.

The situation is quite different along the $\log T = 5.30$ isotherm, where the degree of ionization is high, and atoms are surrounded mostly by charged particles. As discussed in § 3.2.1, the motion of the ions and electrons induce a fluctuating micro-electric field which can cause Stark ionization of the upper levels of the atom, thereby removing them from the IPF. Since this effect is missing in the SC EOS, the IPF retains too many states, and the degree of ionization as well as the internal energy are underestimated. According to Figure 22a, this effect is not very large for $\log \rho \lesssim -2$, but the MHD EOS is nevertheless more accurate in this regime.

Along the $\log T = 5.30$ isotherm, the MHD and the SC EOS differ most notably in the density range $-1 < \log \rho < 1$. On this isotherm, pressure ionization occurs under conditions in which thermal excitation of the atoms is large (see § 3.1). While the MHD model is well beyond its limit of validity

($\log \rho \leq -2$), none of the EOS presented here can be considered truly reliable in this difficult regime.

In Figure 22b, we again find that there is good agreement between the LANL and the SC EOS. Some small differences occur for the hottest two isotherms, as was the case with P . This is somewhat puzzling in a regime where the physics is so simple, but it is not of serious concern. One of the major simplifications employed in the LANL EOS is that each component of the D₂, D, and D⁺ + e mixture is allowed to be nonideal, but they are mixed like an ideal gas. In this approximation, there are no interspecies interactions, and the chemical equilibrium does not depend on the composition. This approximation is closely related to the treatment of the IPF, and the resulting chemical equilibrium is suspect. This effect can be expected to be more pronounced in U than in P , and indeed small deviations from both MHD and SC are found in lowest three isotherms of Figure 22b, even at very low densities.

Such good quantitative agreement between LANL and SC for U and P is surprising, considering the 20 years of improved physical understanding of EOS which separate them. The LANL EOS was developed at a time when the H₂-H₂ potential was poorly known, fluid perturbation theories were in their infancy, and the properties of dense plasmas were just beginning to be explored with numerical simulations. As a consequence, the LANL EOS contains most of the relevant physics, but it is based on very approximate treatments for the nonideal contributions. A good number of ad hoc assumptions and interpolation formulae are used to bridge difficult regimes, and a close look at the model reveals internal inconsistencies between the treatment of bound states and the model for the interactions. For these reasons, we suspect that important differences might be found in the second derivatives of the free energy. Unfortu-

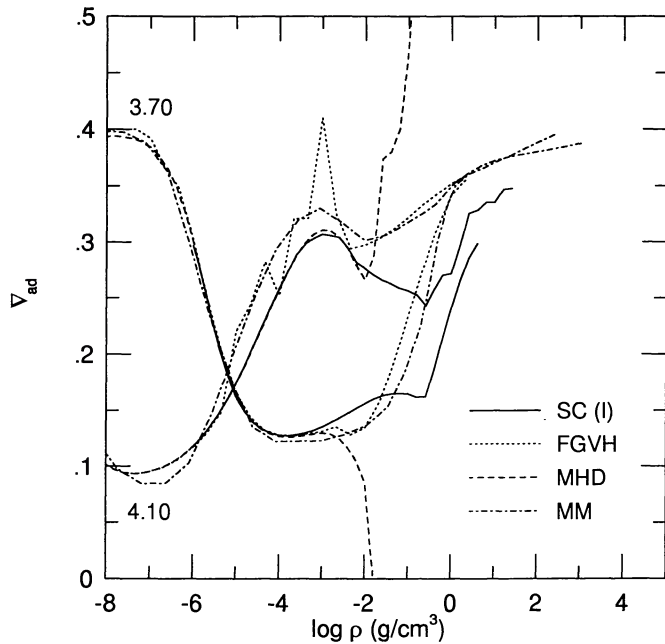


FIG. 23a

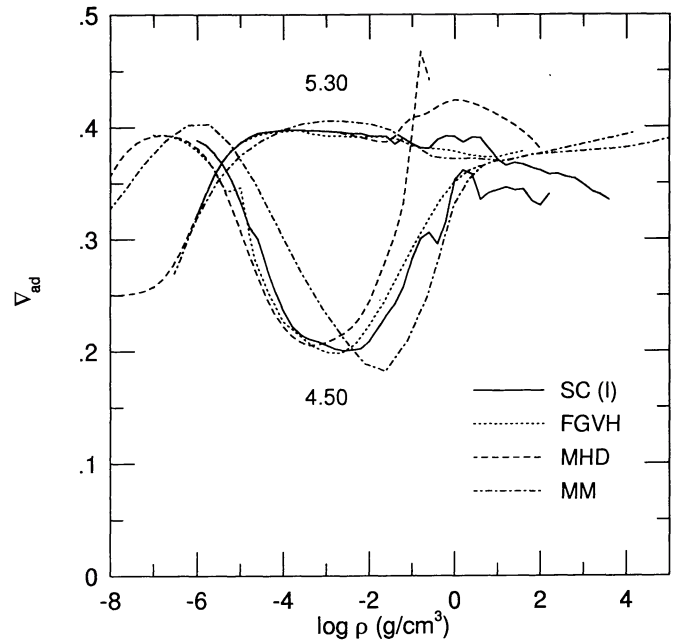


FIG. 23b

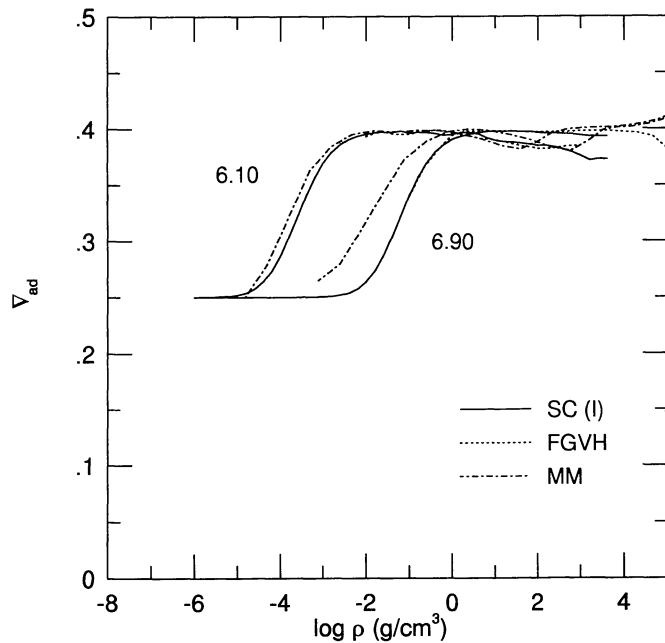


FIG. 23c

FIG. 23.—Comparison of adiabatic gradient isotherms for (a) $\log T = 3.70$ and 4.10 , (b) $\log T = 4.50$ and 5.30 , and (c) $\log T = 6.10$ and 6.90 .

nately, these are not directly available to us, and the process of generating them from the P and U tables may itself introduce significant numerical inaccuracies.

9.1.3. Adiabatic Gradient

The adiabatic temperature gradient is a particularly interesting thermodynamic quantity, as it forms the basis of the Schwarzschild criterion for convective instability in stars.

Comparisons among values for the adiabatic gradient obtained from the MM, MHD, FGVH, and the interpolated SC EOS along each of the six selected isotherms are shown in Figure 23. Figure 10 is helpful in understanding the behavior of Figure 23. Except in a few well known limits, figures of ∇_{ad} are particularly difficult to interpret physically, and we limit the present discussion to a listing of the problems found in each EOS.

Figure 23a shows the lowest isotherms over a wide density range. The overall structure is caused by partial dissociation and ionization, but a number of detailed features are immediately apparent:

1. Even at very low densities, where the gas is ideal, the agreement is not perfect. Differences of 10% are commonplace.
2. The FGVH EOS can be very noisy.
3. The MHD EOS shows pathological behavior for $\log \rho > -2$, once again reinforcing their warning about not using their EOS above this limit.
4. The SC EOS is not smooth in the regime of the fully ionized plasma ($\log \rho > 0.5$).

The next two isotherms are displayed on Fig. 23b. Again, the gross structure seen for $\log T = 4.50$ is due to partial ionization. Hydrogen is nearly fully ionized everywhere along the $\log T = 5.30$ isotherm, and the drop to $\nabla_{ad} = 0.25$ at very low densities is due to the dominance of the photon gas in this regime. We find that

1. There are still significant differences in the ideal gas regime.
2. The FGVH EOS appears smoother in this regime.
3. Above $\log \rho = -1.5$, the MHD EOS shows pathological behavior along both isotherms.
4. For the $\log T = 4.50$ isotherm, the MM EOS shows a "phase lag." This indicates an ionization zone which is displaced to comparatively higher densities and originates from their treatment of the IPF.

5. At the high-density ends of these isotherms, $\Gamma > 10$ and $\theta < 1$, conditions under which the Coulomb interactions are strong. In FGVH and MM, these are described with a Thomas-Fermi-Dirac model, and both show ∇_{ad} rising as the density is increased. On the other hand, SC use a screened one-component plasma model (SOCP; Chabrier 1990), a much more accurate description of the plasma, and find that ∇_{ad} decreases along the isotherm. The SC EOS remains rather noisy in this regime.

Finally, Figure 23c shows the hottest two isotherms. For a pure photon gas, $\nabla_{\text{ad}} = 0.25$, and it approaches 0.4, the value for a noninteracting (ideal), classical, monatomic gas, as the pressure of the plasma comes into play. Both of these limits are readily apparent in this figure. The adiabatic gradient for a mixture of photons and noninteracting protons and electrons can be calculated analytically (Cox & Giuli 1968, § 9.17), a result accurately reproduced by both FGVH and SC; the divergence of the MM curves from the analytic expression cannot be explained on physical grounds. At high densities, ∇_{ad} drops below 0.4 due to weak-to-moderate Coulomb interactions ($\Gamma < 1$). Both the FGVH and SC EOS agree quite well while the MM EOS displays an increase similar to that observed in Figure 23b.

Figure 23 shows differences of as much as 10% in the ideal-gas regime of partial dissociation and ionization, underscoring the sensitivity of ∇_{ad} to the treatment of the states in the IPF. When strong nonideal effects come into play, the adiabatic gradient is a rather poorly determined quantity.

9.2. Comparison along a Solar Interior Profile

Finally, in Figures 24–26, we compare the MHD and SC EOS along the interior profile for the Sun (Däppen 1993; see also curve *c* of Fig. 1). In this case, we consider the appropriate H/He mixing ratio, with $Y = 0.257$ at the surface of the Sun

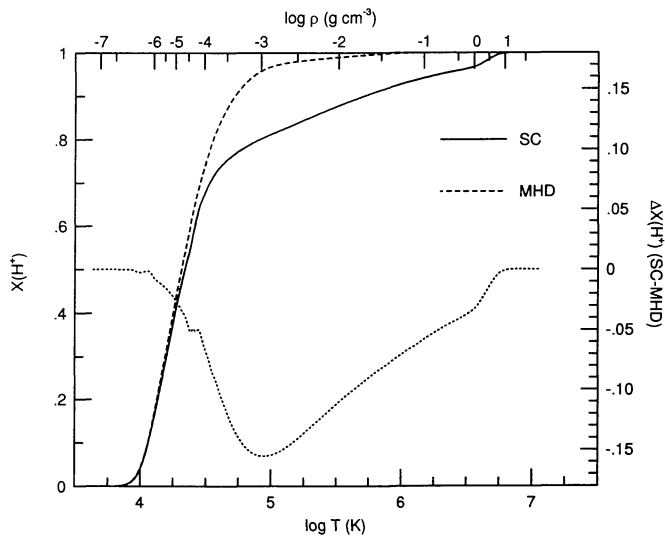


FIG. 24.—Abundance of H^+ for the SC and the MHD EOS along the solar interior profile. The difference is shown by the dotted line, and the scale on the right. The density along this profile is indicated by the top scale.

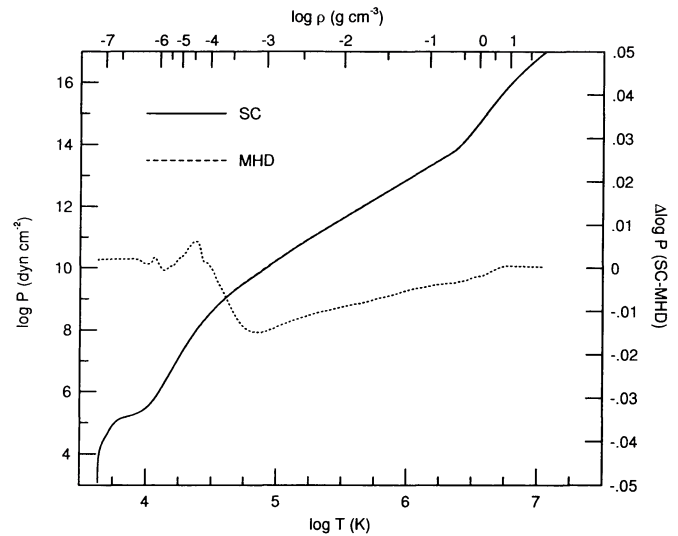


FIG. 25.—Same as Fig. 24 for the gas pressure

and reaching 0.357 at the high-temperature boundary of the SC EOS (near the center).

The degree of ionization of hydrogen along the solar (ρ , T) profile is illustrated in Figure 24. This shows the fraction of all hydrogen species that exist in the form of H^+ . The horizontal scale is linear in $\log T$, and the corresponding density in the solar interior is given by the top scale. There is a significant difference between the prediction of the SC EOS (solid line) and that of the MHD EOS (dashed line). The difference is shown by the dotted curve and can be read off the right-hand scale. This displays dramatically the effect of the microfield on the bound states of the atoms, which favors a higher degree of ionization. Recall that the SC EOS does not include microfield effects, so that the MHD EOS is superior for solar model calculations. Note, however, that this quantity, $X(\text{H}^+)$, accentuates

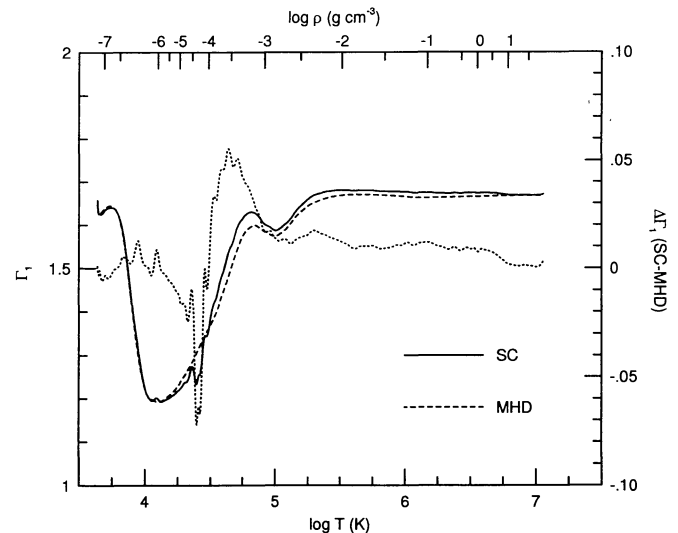


FIG. 26.—Same as Fig. 24 for $\Gamma_1 = \partial \log P / \partial \log \rho|_S$

ates the difference between these EOS. As the following figures show, these differences have relatively small effects on the actual thermodynamic quantities.

The pressure is shown on Figure 25. As expected, in this regime both EOS predict nearly identical pressures, to within a few percent. The dotted curve shows the difference in $\log P$. At intermediate temperatures, the lower degree of ionization in the SC EOS results in a slightly lower pressure, since the particle number density is lower.

Figure 26 shows the adiabatic gradient $\Gamma_1 = \partial \log P / \partial \log \rho|_S$, which is used in pulsation studies. The two troughs in Γ_1 are due to temperature ionization of H and of He, respectively. Due to the relative simplicity of the MHD free-energy model, the second derivatives of F in their EOS are analytic and the EOS is very smooth and free of numerical inaccuracies. We also expect that the MHD EOS has a very high degree of thermodynamic consistency. On the other hand, the SC EOS is somewhat noisier and differs from the MHD result because it underestimates the degree of ionization of hydrogen. The effect on P and Γ_1 , however, is small ($\lesssim 4\%$).

9.3. Other Equations of State

Less detailed comparisons between the SC EOS and additional equations of state used in astrophysical problems have also been performed. The H/He EOS of Marley & Hubbard (1988) was developed for modeling the interior of giant planets. It shares many similarities with the model of SC, and under the low-temperature conditions relevant to giant planets ($\log T < 4$) the two EOS are nearly identical. Differences arise in a narrow density domain centered on pressure ionization, where Marley & Hubbard simply interpolated between the dense molecular fluid and the fully pressure-ionized plasma. For $\log T > 4$, their approximate treatment of temperature ionization leads to substantial disagreement. A more detailed discussion is given in Chabrier et al. (1992).

Rogers (1981) has developed an EOS with an approach entirely different from FMIN, using an activity expansion which considers only protons and electrons interacting through the Coulomb potential. Bound states (atoms) arise naturally in this approach and are not treated as separate chemical species, as in the FMIN method. This approach is rigorous and fundamental (Rogers 1994), but because it is based on an expansion, it fails in regions where the expansion does not converge. Over the (ρ, T) domain where this complex method can presently be solved, it leads to the most accurate EOS currently available. While we have not compared the results of this calculation with the SC EOS, they have been compared with the MHD EOS under conditions appropriate to the solar envelope (see Däppen 1994 & Rogers 1994). The two equations of state are in extremely good agreement, with differences of less than 0.1% in the second derivatives of the free energy. Although such small differences are important when comparing the computed solar oscillation spectrum to the wealth of extremely precise observational data now becoming available, they are completely negligible in all other astrophysical situations. It is most satisfying that two equations of state based on entirely different approaches should agree so well. This indicates that our understanding of the EOS of normal stellar material is now excellent, at least over some parts of the phase diagram.

10. DISCUSSION

We have developed new equations of state for pure hydrogen and pure helium. Because we have treated the nonideal effects carefully, the resulting EOS are particularly appropriate for studies of cool, dense objects such as white dwarf envelopes, low-mass stars, brown dwarfs, and giant planets. The thermodynamic model for hydrogen is quite detailed and has been described extensively in Saumon (1990), SC1, and SC2. This model, summarized in the present paper, addresses the problem of pressure ionization and predicts that it occurs discontinuously through a first-order phase transition, the so-called “plasma phase transition” (PPT). The helium model, however, is simpler, but it is still very reliable over most of the phase diagram. Both EOS are based in part on experimental results, in part on recent progress in the theoretical description of dense plasmas, of fluid mixtures, and of bound states. Both agree very well with a variety of experimental results. We have taken a critical look at the underlying models and at the resulting EOS and point out flaws by considering limiting behaviors, thermodynamic surfaces, and thermodynamic consistency. Equations of state for mixtures of H and He can be approximated by using the additive-volume rule supplemented with an ideal entropy-of-mixing term. Finally, the new EOS is put into perspective by comparing it with several others developed for applications to astrophysical problems (mainly stellar interiors).

This exercise has revealed that the current situation, although quite good in most regimes, is not as satisfactory as is commonly assumed. Much progress has been accomplished over the decades spanned by these EOS. This is due in part to new high-pressure experiments which probe the H_2 - H_2 potential to smaller interparticle separations, in part to the development of a solid understanding of dense plasmas through numerical simulation, and in part to a more acute awareness of the importance of consistency between the treatment of the internal partition function and the interactions between particles.

Each of these EOS has flaws or limitations, most of which can be addressed in the near future. The most challenging areas remain associated with partial dissociation and ionization. The treatment of temperature ionization with the FMIN method has improved considerably in the last few years, but none of the EOS presented here is entirely satisfactory in this regime. The more rigorous activity-expansion technique (Rogers 1981) and the quantum virial expansion (Alastuey 1994; Alastuey et al. 1994) may provide a definitive treatment of temperature ionization. Conversely, pressure ionization remains by far the most poorly understood phenomenon, and a shroud of uncertainty covers that part of the phase diagram, which is important for low-mass stars, brown dwarfs, and, most critically, the Jovian planets.

The comparison of the MHD and SC EOS under conditions appropriate to the solar interior indicates that the SC EOS, although good, is less accurate for this application. The MHD EOS (or the OPAL EOS of Rogers 1981) is a better choice for studies of stars with masses $\gtrsim 1 M_\odot$. However, the SC EOS is preferred for models of low-mass stars, where strong nonideal effects and molecule formation come into play.

The main shortcomings of, and flaws in, the SC EOS—all

discussed here—are well understood. While it does not have a dramatic quantitative effect on the thermodynamics of hydrogen, the fact that the model does not account for the effect of the plasma on the bound levels of the hydrogen atom is its most serious shortcoming. Introduction of a plasma microfield distribution that accounts for plasma coupling and screening (Gilles 1993) is in progress. Similarly, a detailed model for the free energy of helium is being developed (Aparicio & Chabrier 1994).

The four equation-of-state tables, much too extensive to be reproduced here, are presented in the AAS CD-ROM Series, Vol. 5 (1995). These tables are also available by anonymous ftp:

```
%ftp ftp.lpl.arizona.edu
username: anonymous
ftp> cd dsaumon/eos
ftp> mget *
ftp> quit
```

There is one table each for the interpolated hydrogen EOS and for the helium EOS, and two smaller tables are provided for interpolation near the hydrogen plasma phase transition, as explained in §§ 5.2 and 5.3. The first isotherm of the interpolated H EOS table is given in Table 2. Three additional files

provide essential information. The seven files are in ASCII and occupy ~ 1 Mbyte of disk space.

We are most grateful to G. Fontaine and P. Brassard for providing the white dwarf envelope models shown in Figures 1 and 2 and for generating the surface plots for the equation of state (Figs. 4–17). We also thank F. J. Swenson for sending us the $0.3 M_{\odot}$ main-sequence star model for Figure 1. The equation of state comparisons would not have been possible without the collaboration of W. Däppen, D. Mihalas (MHD EOS), and F. D'Antona (MM EOS), who kindly sent us tables at our request. In addition, we are grateful to the Vice Provost for Computing of the University of Rochester and Dr. R. L. McCrory, Director of the University's Laboratory for Laser Energetics, for making available to us the substantial computer resources required to complete the hydrogen EOS calculation. This research was supported in part by NSERC of Canada, by NSF grants AST-8910780 and AST-8914346, by a grant to George H. Rieke from the NASA Origins of the Solar System program (NAGW-2606), and by NASA grant HF-1051.01-93A from the Space Telescope Science Institute, which is operated by the Association of Universities for Research in Astronomy, Inc., under NASA contract NAS5-26555.

REFERENCES

- Alastuey, A. 1994, in IAU Colloq. 147, *The Equation of State in Astrophysics*, ed. G. Chabrier & E. Schatzman (Cambridge: Cambridge Univ. Press), 43
- Alastuey, A., Cornu, F., & Perez, A. 1994, *Phys. Rev. E*, 49, 1077
- Allen, C. W. 1973, *Astrophysical Quantities* (3d ed.; London: Athlone)
- Aparicio, J. M., & Chabrier, G. 1994, *Phys. Rev. E*, 50, 4948
- . 1995, in preparation
- Ashcroft, N. W., & Stroud, D. 1978, *Solid State Phys.*, 33, 2
- Barker, J. A., & Henderson, D. 1976, *Rev. Mod. Phys.*, 48, 567
- Brami, B., Hansen, J. P., & Joly, F. 1979, *Physica A*, 95, 505
- Chabrier, G. 1990, *J. Phys. (Paris)*, 51, 1607
- Chabrier, G., & Ashcroft, N. W. 1990, *Phys. Rev. A*, 42, 6
- Chabrier, G., Saumon, D., Hubbard, W. B., & Lunine, J. 1992, *ApJ*, 391, 817
- Chihara, J. 1991a, *Phys. Rev. A*, 44, 1247
- . 1991b, *Phys. Rev. A*, 44, 8446
- Cox, J. P., & Giuli, R. T. 1968, *Principles of Stellar Structure*, Vol. 1 (New York: Gordon & Breach)
- Däppen, W. 1993, private communication
- . 1994, in IAU Colloq. 147, *The Equation of State in Astrophysics*, ed. G. Chabrier & E. Schatzman (Cambridge: Cambridge Univ. Press), 368
- Däppen, W., Mihalas, D., Hummer, D. G., & Mihalas, B. W. 1988, *ApJ*, 332, 261
- DeWitt, H. E. 1961, *J. Nucl. Energy, C*, 2, 224
- Dorman, B., Irwin, A. W., & Pedersen, B. B. 1991, *ApJ*, 381, 228
- Duffy, T. S., Vos, W. L., Zha, C-s, Hemley, R. J., & Mao, H-k 1994, *Science*, 263, 1590
- Ebeling, W., & Richert, W. 1985, *Phys. Lett., A*, 108, 80
- Farouki, R. T., & Hamaguchi, S. 1994, *Phys. Rev. E*, 101, 9876
- Fontaine, G., Graboske, H. C., Jr., & Van Horn, H. M. 1977, *ApJS*, 35, 293
- Gilles, D. 1993, private communication
- Graboske, H. C., Jr., Harwood, D. J., & Rogers, F. J. 1969, *Phys. Rev.*, 186, 210
- Harris, G. M. 1959, *J. Chem. Phys.*, 31, 1211
- Harris, G. M., Trulio, J., & Roberts, J. 1960, *Phys. Rev.*, 119, 1832
- Holmes, N. C., Ross, M., & Nellis, W. J. 1995, *Phys. Rev. B*, submitted
- Hubbard, W. B., & DeWitt, H. E. 1985, *ApJ*, 290, 388
- Hummer, D. G., & Mihalas, D. 1988, *ApJ*, 331, 794
- Ichimaru, S., Iyetomi, H., & Tanaka, S. 1987, *Phys. Rep.*, 149, 91
- Kerley, G. I. 1972, *Phys. Earth Planet. Interiors*, 6, 78
- Kraeft, K. D., Kremp, D., Ebeling, W., & Röpke, G. 1986, *Quantum Statistics of Charged Particle Systems* (New York: Plenum)
- Lamb, D. Q. 1974, Ph.D. thesis, Univ. of Rochester
- Lamb, D. Q., & Van Horn, H. M. 1975, *ApJ*, 200, 306
- Landau, L. D., & Lifshitz, E. M. 1980, *Course of Theoretical Physics*, Vol. V., *Statistical Physics, Part 1* (3d ed.; Oxford: Pergamon)
- Landau, L. D., & Zeldovich, Ya. B. 1943, *Acta Phys.-Chim. USSR*, 18, 194
- Magni, G., & Mazzitelli, I. 1979, *A&A*, 72, 134
- Mao, H-k, & Hemley, R. J. 1992, *Am. Scientist*, 80, 234
- Marley, M. S., & Hubbard, W. B. 1988, *Icarus*, 73, 536
- Mazzitelli, I. 1993, private communication
- . 1994, in IAU Colloq. 147, *The Equation of State in Astrophysics*, ed. G. Chabrier & E. Schatzman (Cambridge: Cambridge Univ. Press), 144
- Mihalas, D., Däppen, W., & Hummer, D. G. 1988, *ApJ*, 331, 815
- More, R. M. 1976, *J. Phys. A*, 9, 1979
- Nellis, W. J., Holmes, N. C., Mitchell, A. C., Trainor, R. J., Governo, G. K., Ross, M., & Young, D. A. 1984, *Phys. Rev. Lett.*, 53, 1248
- Perrot, F., & Dharma-wardana, M. W. C. 1994, in IAU Colloq. 147, *The Equation of State in Astrophysics*, ed. G. Chabrier & E. Schatzman (Cambridge: Cambridge Univ. Press), 272
- Perrot, F., Furutani, Y., & Dharma-wardana, M. W. C. 1990, *Phys. Rev. A*, 41, 1097
- Press, W. H., Flannery, B. P., Teukolsky, S. A., & Vetterling, W. T. 1986, *Numerical Recipes* (Cambridge: Cambridge Univ. Press)
- Reichl, L. E. 1980, *A Modern Course in Statistical Physics* (Austin: Univ. of Texas)
- Rogers, F. J. 1981, *Phys. Rev. A*, 24, 1531
- . 1984, *Phys. Rev. A*, 29, 868
- . 1994, in IAU Colloq. 147, *The Equation of State in Astrophysics*, ed. G. Chabrier & E. Schatzman (Cambridge: Cambridge Univ. Press), 16
- Ross, M. 1979, *J. Chem. Phys.*, 71, 1567
- Ross, M., Ree, F. H., & Young, D. A. 1983, *J. Chem. Phys.*, 79, 1487
- Saumon, D. 1990, Ph.D. thesis, Univ. of Rochester

- Saumon, D., & Chabrier, G. 1991, *Phys. Rev. A*, 44, 5122 (SC1)
———. 1992, *Phys. Rev. A*, 46, 2084 (SC2)
- Saumon, D., & Van Horn, H. M. 1987, in *Strongly Coupled Plasma Physics*, ed. F. J. Rogers & H. E. DeWitt (New York: Plenum), 173
- Smith, W. R., & Henderson, D. 1970, *Molec. Phys.*, 19, 411
- Stevenson, D. J. 1975, *Phys. Rev. B*, 12, 3999
- Stevenson, D. J., & Salpeter, E. E. 1977, *ApJS*, 35, 221
- Stolzman, W., & Blocker, T. 1994, in *IAU Colloq. 147, The Equation of State in Astrophysics*, ed. G. Chabrier & E. Schatzman (Cambridge: Cambridge Univ. Press), 606
- Tanaka, S., Yan, X-Z, & Ichimaru, S. 1990, *Phys. Rev. A*, 41, 5616
- Verlet, L., & Weis, J. J. 1972, *Phys. Rev. A*, 5, 939
- Weeks, J. D., Chandler, D., & Anderson, H. C. 1971a, *J. Chem. Phys.*, 54, 5237
———. 1971b, *J. Chem. Phys.*, 55, 5422
- Wigner, E., & Huntington, H. B. 1935, *J. Chem. Phys.*, 3, 764